Received: 15 February 2025 | Revised: 7 August 2025 | Accepted: 18 September 2025

DOI: 10.1002/dep2.70045

The Depositional Record
Open Access
A journal of the International Association of Sedimentologists
IAS
WILEY

ORIGINAL ARTICLE

Orbital and eustatic control of basin hydrology during the first stage of the Messinian Salinity Crisis

Fernando Gázquez[1,2,3] | **Nicholas P. Evans**[1] | **Thomas K. Bauska**[1,4] | **Harold J. Bradbury**[1,5] | **Alexandra V. Turchyn**[1] | **María del Carmen Barroso**[1] | **Alexander M. Piotrowski**[1] | **José María Calaforra**[2,3] | **David A. Hodell**[1]

[1]Godwin Laboratory for Palaeoclimate Research, Department of Earth Sciences, University of Cambridge, Cambridge, UK

[2]Department of Biology and Geology, Universidad de Almería, Almería, Spain

[3]Andalusian Centre for Global Change-Hermelindo Castro (ENGLOBA), University of Almería, Almería, Spain

[4]British Antarctic Survey, Cambridge, UK

[5]Department of Earth, Ocean and Atmospheric Sciences, University of British Columbia, Vancouver, British Columbia, Canada

Correspondence
David A. Hodell, Godwin Laboratory for Palaeoclimate Research, Department of Earth Sciences, University of Cambridge, Downing Street, Cambridge CB2 3EQ, UK.
Email: dah73@cam.ac.uk

Funding information
European Reseach Council, Grant/Award Number: 339694; Ministerio de Ciencia e Innovación, Grant/Award Number: PID2021-123980OA-I00 and RYC2020-029811-I; Universidad de Almería, Grant/Award Number: RyC-PPI2021-01

Abstract

Gypsum and marls from the 15 cycles of the Messinian Yesares Member in the Sorbas Basin, SE Spain, were analysed using a multi-isotope approach to reconstruct palaeo-hydrological conditions of the basin and the wider Mediterranean region during the deposition of the Primary Lower Gypsum (PLG) of the Messinian Salinity Crisis (MSC) (~5.97–5.60 Ma). By analysing structurally-bound water in sedimentary gypsum ($CaSO_4{\cdot}2H_2O$), the past oxygen and hydrogen isotopic composition of waters during evaporite formation is determined. These measurements are combined with water salinity inferred from gypsum fluid inclusions and isotopic analysis of strontium ($^{87}Sr/^{86}Sr$), calcium ($\delta^{44}/^{40}Ca$), sulphur ($\delta^{34}S$) and oxygen of sulphate ($\delta^{18}O_{SO_4}$) in the same samples, as well as isotopic analysis ($\delta^{44}/^{40}Ca$, $^{87}Sr/^{86}Sr$, $\delta^{18}O_{carb}$, $\delta^{13}C$) of the interbedded carbonate marls. The PLG in the Sorbas Basin did not form solely from the evaporation of seawater but rather precipitated from a hybrid brine consisting of seawater and a significant input of freshwater. The seawater/freshwater ratio changed through time and was influenced by (1) tectonic uplift and basin restriction, (2) obliquity-driven glacial–interglacial sea level changes and (3) precession-driven freshwater influx. A progressive freshwater increase up-section reflects tectonic restriction of the basin, supported by $^{87}Sr/^{86}Sr$ trends, which start at seawater values in Cycle 2 and deviate upward. Two minor reversals in $^{87}Sr/^{86}Sr$ at ~5.84 and ~5.72 Ma reflect the role of obliquity-controlled sea level and eccentricity-modulated precession. Maximum divergence of $^{87}Sr/^{86}Sr$ from the seawater curve, as well as precipitation of authigenic dolomite with high $\delta^{18}O_{carb}$, represent a temporary regime change to a freshwater-dominated system coincident with the strongest glacial stages (Marine Isotope Stage TG20) and an eccentricity minimum at ~5.75 Ma. A gradual tectonic restriction of the Atlantic connection, superimposed on orbitally controlled glacio-eustatic (obliquity-dominated) and freshwater input (precession-dominated) changes, led to gypsum-marl deposition in Mediterranean marginal basins during the early MSC.

KEYWORDS

calcium isotopes, evaporites, gypsum hydration water, Messinian Salinity Crisis, Sorbas Basin, strontium isotopes, triple oxygen isotopes

1 | INTRODUCTION

Almost five decades ago, Deep Sea Drilling Project Leg 13 in the Mediterranean uncovered physical evidence for the Messinian Salinity Crisis (MSC) beneath the seafloor of the Mediterranean Sea. During the MSC, over 1 million km^3 of evaporitic minerals were deposited (Hsü et al., 1973; Ryan et al., 1973), making it the most recent of the salt giants (Krijgsman et al., 2024). Subsequent research led to the formulation of a consensus stratigraphic model (CIESM, 2008; summarised by Roveri et al., 2014), which subdivides evaporite deposition into three major evolutionary stages: During Stage 1, interbedded gypsum and carbonate marls were deposited representing the Primary Lower Gypsum; PLG; (~5.97–5.60 Ma); Stage 2 followed with the deposition of kilometre-thick sequences of halite in deep Mediterranean basins (5.60–5.55 Ma); and finally, Stage 3 was characterised by gypsum-marl sequences in both deep (Upper Unit; Lofi et al., 2011) and intermediate settings (Upper Gypsum; UG; ~5.55–5.42 Ma) and brackish deposits (Lago Mare; ~5.42–5.33 Ma). The degree to which the CIESM model is applicable to the entire Mediterranean basin is a topic of active debate.

The Sorbas Basin (southeastern Spain) preserves a record of the early phase of the MSC (5.97–5.6 Ma) in which the Primary Lower Gypsum, consisting of gypsum-marl cycles, was deposited in a silled marginal basin. This basin has become a type locality for the onset and early stage of cyclic evaporite deposition (Modestou et al., 2017; Reghizzi et al., 2017). Up to 16 gypsum-marl cycles were deposited, which vary in thickness and lithology and constitute the Yesares Member of the Sorbas Basin (Roveri et al., 2009). Questions remain about the factors that influenced the precipitation of gypsum and marl, as well as the primary ion source during each depositional cycle.

Previous studies utilising isotope tracers, such as strontium ($^{87}Sr/^{86}Sr$), sulphur ($\delta^{34}S$), and oxygen isotopes in sulphate ($\delta^{18}O_{SO_4}$), suggested that the deposition of the PLG occurred under normal marine conditions with a permanent connection between the Mediterranean and the Atlantic, driven by astronomically controlled climatic oscillations (e.g. Krijgsman et al., 1999, 2024; Longinelli, 1979; Lu & Meyers, 2003; Lugli et al., 2010; Manzi et al., 2013; Müller & Mueller, 1991; Roveri et al., 2014). However, the average freshwater contribution during the PLG remains uncertain owing to the limited sensitivity of traditional isotope tracers (e.g., Sr and S isotope ratios) to continental water input, as rivers contribute only minor amounts of Sr and SO_4^{2-} compared to seawater (Lu & Meyers, 2003; Rossi et al., 2015). Some studies suggest Mediterranean salinity may have been lower than the saturation horizon at which gypsum precipitation occurs (~130 $g\,L^{-1}$) during the evaporation of seawater alone (e.g. Aloisi et al., 2022; Dela Pierre et al., 2014; Evans et al., 2015; Natalicchio et al., 2014; Rosell et al., 1998; Rossi et al., 2015). Because of difficulties reconstructing both palaeosalinity and the relative influence of freshwater water contributions to the PLG gypsum-carbonate cycles (e.g. Lu & Meyers, 2003; Rossi et al., 2015), neither the magnitude nor the timing of salinity changes in the Mediterranean basin is well constrained (Flecker et al., 2015). Additionally, the correlation between the variability of stable isotopes in marginal basin waters (i.e. oxygen and hydrogen isotopic composition of water and dissolved solutes, such as $^{87}Sr/^{86}Sr$ and $\delta^{34}S_{SO_4}$) with eustatic sea-level changes and orbital forcing remains tentative and requires further investigation (Krijgsman et al., 2024).

In the present study, a PLG cycle is defined as a double layer of gypsum overlain by a marl layer, which serves as the base for the next gypsum–marl cycle. A multi-isotope study of 15 cycles of gypsum-marl deposition comprising the Yesares Member, Sorbas Basin, was conducted to constrain the evolving hydrological conditions during the early stage of the MSC. In addition to $^{87}Sr/^{86}Sr$, $\delta^{34}S$ and $\delta^{18}O_{SO_4}$ isotope analysis of gypsum, the triple oxygen and hydrogen isotope ratios of gypsum hydration water (GHW) were measured, along with calcium isotope ratios of the gypsum ($\delta^{44}/^{40}Ca$) and salinity deduced from fluid inclusions. Previous work has shown that $^{87}Sr/^{86}Sr$ (e.g. Flecker et al., 2002; Topper & Meijer, 2013) and stable isotopes of GHW can be used to constrain the hydrological budget of a basin (Gázquez et al., 2018; Gázquez & Hodell, 2022; Herwartz et al., 2017), its connection with the open ocean and mixing with non-marine waters (Aloisi et al., 2022; Evans et al., 2015, 2018).

Evans et al. (2015) measured a single cycle of the Yesares Member at the base of Rio de Aguas section (identified as cycle 6 by these authors and designated as cycle 10 in the present study; see section 2 in Supplement for redesignation rationale). They found evidence for a significant and changing influence of meteoric water throughout the cycle of gypsum-marl deposition. In this study, we expanded the work to include gypsum and marls from the 15 cycles of the PLG in the Sorbas Basin. The objectives were to: (1) evaluate the contribution of freshwater during the formation of the PLG; (2) to investigate orbital forcing of Messinian climate on the geochemistry of Mediterranean seawater and (3) to better understand the sedimentary environments in which marginal gypsum deposits formed during the MSC. This study provides multiple sources of information on the parent water from which gypsum precipitated and will be useful for future work to quantify water/solute fluxes between the Sorbas Basin and the open Mediterranean, using numerical isotope mass balance models (e.g. Aloisi et al., 2022; Gázquez et al., 2018; Topper et al., 2014).

2 | GEOLOGICAL SETTING: THE SORBAS BASIN, SE SPAIN

The Neogene Sorbas Basin is an elongated intra-montane depression surrounded by basement highs of the Betic Internal Zone (Figure 1). It preserves the transition from the marine marls of the Upper Abad Member to the Yesares Formation composed of interbedded gypsum and marls (Krijgsman et al., 2001), representing the PLG and Stage 1 of the MSC. It represents a key area for understanding the Western Mediterranean palaeoceanographic evolution during the onset of the MSC (Reghizzi et al., 2017).

The Yesares Member occurs within a ~160 m thick sequence consisting of gypsum-marl cycles that have been astronomically tuned to precession (e.g. Krijgsman et al., 1999, 2001; Lugli et al., 2010; Roveri et al., 2009). The selenitic gypsum units are up to 30 m thick. Dronkert (1985) was the first to describe the sedimentary cycles of the Yesares Member of the Sorbas Basin, reporting 12 cycles of alternating gypsum and carbonate-marl. In subsequent studies; however, the reported stratigraphic order and number of cycles of the Yesares Member have increased from this original interpretation. Rosell et al. (1998) described 13 cycles in their stratigraphic log of the Los Molinos section, whereas Krijgsman et al. (2001) described 14 cycles in the same section. Lugli et al. (2010) and Roveri et al. (2009) reported 15 and 16 cycles, respectively, although these studies interpret the basal cycle of the Los Molinos section to be cycle 2. This is because 'cycle 1', a carbonate-sapropel couplet that occurs at the base of this locality, has been correlated more recently with a gypsum cycle at the base of the Perales section (Manzi et al., 2013). As well as the addition of this cycle at the bottom of the PLG, the variable number of total cycles described is likely related to the differing interpretation of the upper half of the Los Molinos section where outcropping gypsum/limestone units are thin and obscured.

The lower 5 cycles consist of thick gypsum beds (30 to 15 m) interbedded with thin marl strata (0.5–2 m). The gypsum beds are significantly thinner beginning with cycle 6 and are generally less than 6 m thick from cycle 10. The mislabelled sixth cycle described by Evans et al. (2015) is now cycle 10. The contact between the marl and the overlying gypsum in cycles 3–10 is undulating and contains "nucleation cones" (Dronkert, 1985), which are not present in the lowermost and uppermost cycles. These load structures consist of conical clusters of crystals that occur at the base of the gypsum beds, representing the initial nucleation points of gypsum that sank into the relatively soft marls (Lugli et al., 2010). The presence of seven syndepositional load structures at the contact between gypsum and the underlying marls ("nucleation cones"), as well as the thickness of the gypsum-marl beds, allows for correlation among the different outcrops (Figure 1). The uppermost cycles contain meter-thick beds of selenite interbedded with distinct layers of carbonate marls (up to 30 cm thick). The thickness of the gypsum units generally decreases upsection (Ryan & Raad, 2025), and the stacking pattern of the gypsum-marl cycles in the Sorbas Basin is similar to those offshore (Ochoa et al., 2015).

Here, the cyclicity and stratigraphic sequence of the Yesares Member in outcrop and subsurface of the Sorbas Basin is reinvestigated (Figure 1 and Figure S1). This study focuses on the Cueva del Agua section (37°06′27″N; 02°02′43″W, gypsum from cycle 1), the Perales section at the Majadas Viejas quarry (37°05′03″N; 02°05′20″W, gypsum-marls from cycle 2), the passages of Covadura Cave (Bosque branch; 37°07′22″N; 02°04′08″W; Gázquez et al., 2016; Gázquez, Calaforra, et al., 2017; gypsum-marls from cycles 3 to 7 and gypsum from cycle 8); the Río de Aguas section (37°05′23″N; 02°06′54″W; marls from cycle 9, gypsum-marls from cycles 10, and gypsum from cycle 11); the Barranco del Infierno section (37°04′58″N; 02°07′07″W; marls from cycles 12 and gypsum-marls from cycle 13); and the Los Molinos section (37°06′19″N; 02°04′44″W; marls from cycle 14 and gypsum-marls from cycle 15) (Figure 1). In addition, samples of pre-MSC carbonates from the Perales section (upper Abad marls carbonates at the contact with the PLG1 gypsum; 37°05′57.06″N; 02°03′14.64″W) were collected. Our field surveys indicate that 12 distinct gypsum-carbonate cycles are present in the wider basin, whereas an additional three gypsum-carbonate cycles are present in the uppermost part of the Los Molinos section. Cycles 9 and 14 were not sampled for gypsum, and cycles 1 and 8 were not sampled for carbonate minerals because these beds were not safely accessible in the sections studied.

The lowermost gypsum bed is located at the Cueva del Agua section, where the contact with the underlying Abad marls is observed. Manzi et al. (2013) recognised this highly discontinuous gypsum bed within the 'transitional interval' at the Abad/Yesares boundary (Sierro et al., 2001) below the lowermost continuous gypsum layer (i.e. cycle 2). The subsequent two cycles are exposed at the Majadas Viejas quarry (Perales section), displaying massive selenite crystals generally larger than 10 cm, with little crystal size variation. Cycles 3–8 can be observed in the passages of Covadura Cave. The sixth cycle marks the first appearance of "supercones" and the stratigraphic order in the Covadura Cave is generally recognisable in the lower half of the Los Molinos section. The upper part of the Yesares Member is best exposed in the Rio de Aguas and Barranco del Infierno sections, where the transition into the lowermost Sorbas Member is also exposed (Krijgsman et al., 2001). Eight distinct gypsum cycles are present in the Barranco del

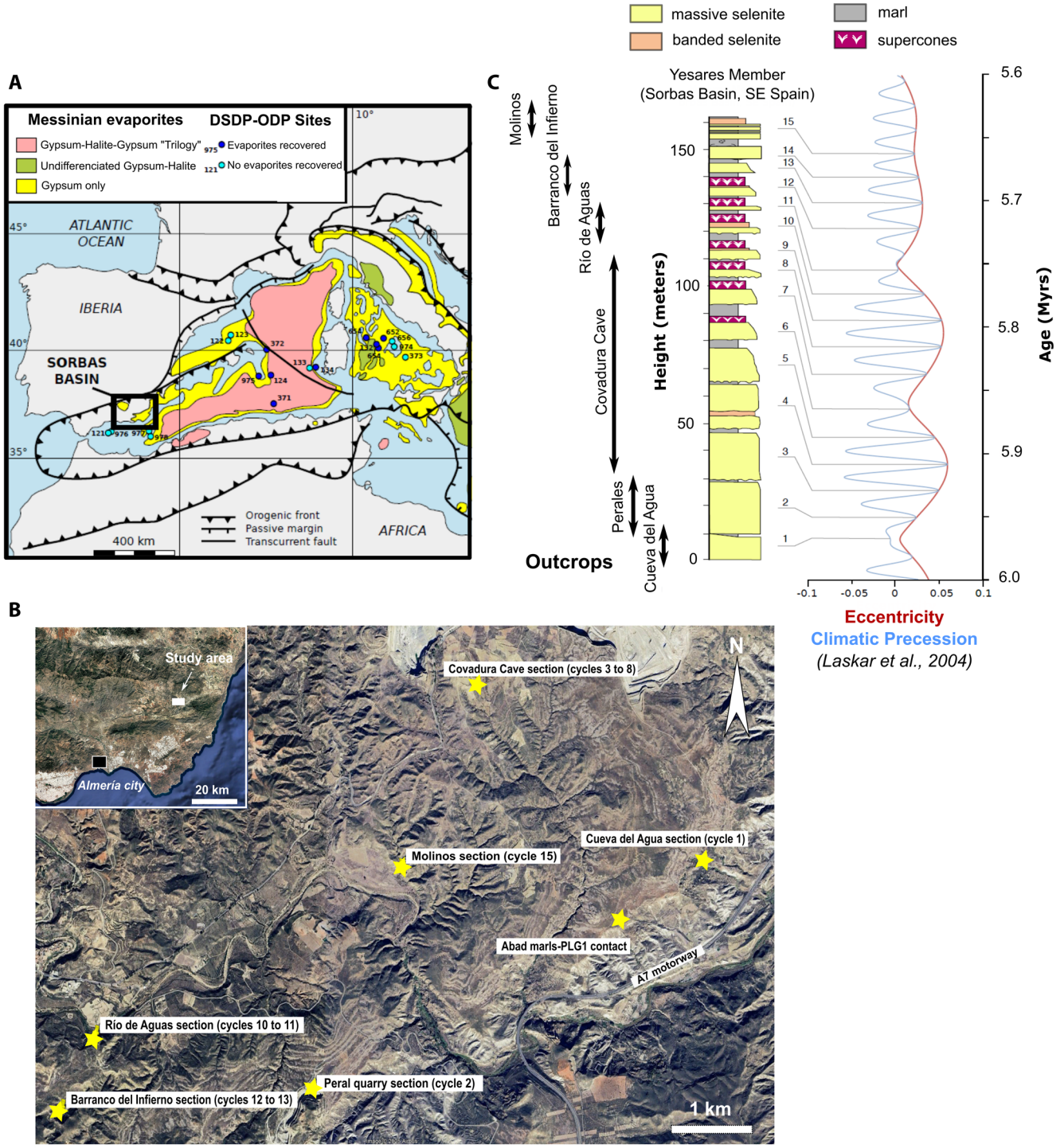

FIGURE 1 (A) Map of the Messinian evaporites in the western Mediterranean and the Sorbas Basin. Also shown is the location of the DSDP-ODP boreholes where Messinian evaporites were recovered (e.g. Hsü et al., 1973; Ryan et al., 1973), as well as other PLG sections found in marginal basin settings. (B) Location of the study area and the sampling sites (see main text for geographic coordinates). (C) Astronomical tuning of the PLG units in the Yesares member of the Sorbas Basin adopted in this study, consisting of cycles exposed at the five sections investigated in this study (Rio de Aguas, Los Molinos, Perales, Covadura Cave and Barranco del Infierno). The detailed logs of the sections are given in Figure S1.

Infierno section; the uppermost gypsum cycle is a relatively discontinuous layer consisting of massive selenite, whereas the lower seven cycles in this section display both massive selenite and supercone structures. The eight cycles of the Barranco del Infierno section correspond to cycles 6–13, as revealed by the presence

of seven cycles containing supercones. The three cycles exposed at the base of the Rio de Aguas section also contain supercone structures and are overlain by a discontinuous gypsum/carbonate unit.

These cycles at Rio de Aguas are recognisable as the lateral equivalent of the upper part of the Barranco del Infierno section, thus corresponding to evaporite cycles 10–12. Dronkert (1985) observed a similar correlation between the Rio de Aguas and Barranco del Infierno sections, although he incorrectly correlated the cycles to the Los Molinos section and did not log the discontinuous gypsum layer above the uppermost supercone cycle. The uppermost part of the Los Molinos section contains two further gypsum-carbonate cycles. The carbonate-marl couple below the uppermost gypsum layer displays signs of slumping. As the two uppermost cycles of the Los Molinos section are not present in the Rio de Aguas and Barranco del Infierno sections, the beds may not be laterally continuous across the basin.

3 | MATERIALS AND METHODS

3.1 | Sample collection methods

Individual gypsum crystals ($n = 114$) were removed using a hammer and chisel from the outcrops of cycles 1–8, 10–13, and 15, with different sampling resolutions. Cycles 2, 7, 10, and 12 were subject to high-resolution sampling, whereby >22 discrete, evenly spaced gypsum samples were analysed in each cycle. Carbonate samples ($n = 129$) were taken using a battery-powered drill fitted with a coring drill bit from outcrops of cycles 1, 3–7, and 9–15. The corer was inserted parallel to the bedding plane after removal of the outer 5 cm of marl to avoid contamination. The positions of the samples in each section are shown in Figure S1, and their exact heights within the cycle and the complete log are provided in Table S1.

To constrain potential sources of riverine strontium and their isotopic composition during the MSC in the Sorbas Basin, water samples for Sr concentration and $^{87}Sr/^{86}Sr$ analyses from 4 springs in the Sierra de los Filabres mountain range (northwest of the Sorbas Basin) were collected: 2 springs in limestone and 2 springs in schists (see Table S1 for geographical locations).

3.2 | Mineralogical analyses

X-ray diffraction (XRD) analysis was conducted on carbonate samples to estimate the relative proportion of calcite to dolomite in the sample with a D8 Bruker diffractometer equipped, using a Cu Kα X-ray source at the Department of Earth Sciences at the University of Cambridge (United Kingdom). The accuracy is ±1%–2% for major phases (see Supporting Information for details).

3.3 | Stable isotope analyses

3.3.1 | Gypsum hydration water

Triple oxygen and hydrogen isotopes of GHW were analysed using the method described by Gázquez et al. (2015) in the Godwin Laboratory of the Department of Earth Sciences at the University of Cambridge (see Supporting Information for details). The external reproducibility of the method (1σ) was ±0.1‰ for $\delta^{17}O$, ±0.2‰ for $\delta^{18}O$, and ±0.8‰ for δD, ±1‰ for d-excess, and ±12 per meg for ^{17}O-excess, estimated by measurement of an internal gypsum standard ($n > 200$) during the 2-year period in which the samples were analysed. The $\delta^{17}O$, $\delta^{18}O$, and δD of the mother water from which the gypsum precipitated is calculated by correcting the measured isotopic values for the gypsum-water fractionation factors (Gázquez, Evans, & Hodell, 2017). Fractionation factors of 1.00341 and 0.981 for oxygen ($\alpha^{18}O_{gypsum\text{-}water}$) and hydrogen isotope ratios ($\alpha D_{gypsum\text{-}water}$), respectively, were used at a water temperature of ~15–20°C and salinity of <150 g L^{-1}, based on temperature data and the salinity deduced from fluid inclusions by Evans et al. (2015). A θ value of 0.5297 for the triple oxygen isotope relationship ($\alpha^{17}O_{gypsum\text{-}water} = \alpha^{18}O_{gypsum\text{-}water}{}^{\theta}$) was used (Gázquez et al., 2017). The sensitivity of the fractionation factors to temperature is low, especially for oxygen isotopes (Gázquez et al., 2017; Liu et al., 2019). Following correction of the $\delta^{17}O$, $\delta^{18}O$, and δD of the gypsum mother water, the derived parameters d-excess and ^{17}O-excess were calculated.

3.3.2 | Sulphur, oxygen ($\delta^{18}O_{SO_4}$), strontium, and calcium isotopes of gypsum

For analysis of the sulphur and oxygen isotopic composition of the sulphate in gypsum, the samples were dissolved in distilled water and SO_4^{2-} reprecipitated as $BaSO_4$. Sulphur isotope ratios were measured using a ThermoScientific Delta V Plus isotope ratio mass spectrometer coupled via continuous flow to a Flash Element Analyser at the University of Cambridge (see Supporting Information for additional details). Oxygen isotope ratios in sulphate ($\delta^{18}O_{SO_4}$) were measured using a Thermal Combustion Element Analyser (TC/EA) coupled via continuous flow to a Delta V isotope ratio mass spectrometer. All $\delta^{18}O_{SO_4}$

are reported relative to V-SMOW (Vienna-Standard Mean Ocean Water), with typical standard deviation better than ±0.5‰ (1σ) based on replicate analyses. All $\delta^{34}S$ values are reported relative to VCDT (Vienna-Canyon Diablo Troilite) and the long-term reproducibility was better than ±0.2‰ (1σ).

The Sr/Ca ratios in gypsum samples were determined by ICP-OES after dilution in 0.1 M HNO_3 to a constant calcium concentration of between 10 ppm and 50 ppm. Samples were run on a Varian Vista Axial ICP-OES at the Department of Earth Sciences of the University of Cambridge, using the 315.887 nm Ca emission line. In-house calibration standards were prepared to closely match the concentration matrix of the media solutions. The Sr content in spring waters was determined using the same instrument that also produced also results of Ca, Mg, Na, and S concentrations (see Table S1).

For analysis of strontium isotope ratios in gypsum ($^{87}Sr/^{86}Sr$), strontium was purified using column chemistry, and the purified fractions were measured by thermal ionisation mass-spectrometry (Thermo-Scientific Triton Plus MC-TIMS) at the University of Cambridge, with a long-term precision of ±0.000007 (2σ) (see Supporting Information for additional details). Calcium isotope ($^{44}Ca/^{40}Ca$) analysis was conducted using a Thermo Scientific Triton Plus MC-TIMS, using a 42–48 double spike, closely following the method of Bradbury and Turchyn (2018) and Bradbury et al. (2018) and is reported relative to Bulk Silicate Earth (BSE) (mean = −0.28, n = 82) (see Supporting Information for additional details). The average external 2σ standard deviation over 9 months on the standard NIST915B was ±0.10‰. The analyses of $^{87}Sr/^{86}Sr$ in carbonates followed the same protocol as for gypsum.

3.4 | Total inorganic carbon, $\delta^{18}O_{carb}$ and $\delta^{13}C$ of bulk carbonates

Weight percent (wt%) carbonate was measured by digesting homogenised samples in 10% H_3PO_4 for 20 min at 70°C, and total inorganic carbon was measured using an AutoMateFX autosampler coupled to a UIC (Coulometrics) 5011 CO_2 coulometer (Engleman et al., 1985), with analytical precision better than 1% (see Supporting Information for additional details). For stable isotope analysis of carbonate, bulk sediment samples were acidified with 104% H_3PO_4, and stable carbon and oxygen isotopes of CO_2 were measured using a Thermo Scientific GasBench II, equipped with a CTC autosampler coupled to a MAT253 mass spectrometer (Spötl & Vennemann, 2003), with precision of ±0.08‰ for $\delta^{13}C$ and ± 0.1‰ for $\delta^{18}O_{carb}$. Results are reported relative to the VPDB (see Supporting Information for additional details).

3.5 | Fluid inclusion microthermometry

The method closely followed that described by Attia et al. (1995) and Evans et al. (2015). Thin (<1 mm) samples of gypsum were obtained by cleaving the mineral along the 010 plane using a razor blade. The fragments were placed in a Linkam THMSG600 heating-freezing stage attached to a Zeiss Axio Scope.A1 microscope equipped with a 100× objective at the Department of Earth Sciences of the University of Cambridge. The samples were frozen to −90°C and then heated at a rate of 1°C per minute to room temperature. Tm_{ice} was recorded to within 0.1°C and reproduced at least twice for each inclusion with an error of ±0.2°C. Salinities of the fluid inclusions were calculated from the final melting temperatures of ice and expressed as both weight % NaCl equivalent (Bodnar, 1993) and parts per thousand (Goldstein & Reynolds, 1994).

4 | RESULTS

4.1 | Gypsum Hydration Water

4.1.1 | Inter-cycle trends

The range of $\delta^{18}O$ and δD does not vary greatly among gypsum cycles, with little change up-section (Figure 2). Mean (±1σ) $\delta^{18}O$ and δD values of gypsum hydration water corrected for isotopic fractionation factors are 0.99 ± 1.5‰ and 1.1 ± 9.6‰, respectively, across the entire section. The lowest mean $\delta^{18}O$ and δD values occur in cycle 5 ($\delta^{18}O$ = −1.1‰; δD = −13.3‰) and cycle 11 ($\delta^{18}O$ = −0.1‰; δD = −6.2‰). The highest mean intra-cycle values occur in cycle 8 ($\delta^{18}O$ = 2.1‰; δD = 9.0‰) and cycle 13 ($\delta^{18}O$ = 1.9‰; δD = 7.1‰). Deuterium excess is also relatively constant across all gypsum cycles with a mean (±1σ) value of −6.8 ± 3.0‰. ^{17}O-excess is −44 ± 6 per meg at the base of cycle 1 but rises to a mean value of −19 ± 9 per meg over cycles 2–11. In cycles 12–15, ^{17}O-excess returns to lower values (−37 ± 13 per meg), similar to cycle 1. The d-excess and ^{17}O-excess are also negatively correlated with $\delta^{18}O$ and δD (Figure 3); the most positive mean intra-cycle values occur in cycle 5 (d-excess = −1.1‰; ^{17}O-excess = −13 per meg) and cycle 12 (d-excess = −0.1‰; ^{17}O-excess = −16 per meg). The corrected gypsum hydration water isotopic results define an evaporative line: $\delta D = 6.29 * \delta^{18}O - 5.08$ (R^2 = 0.97) that intercepts the Local Meteoric Water Line (LMWL) near the average value of rainwater in Sorbas (Gázquez, Calaforra, et al., 2017).

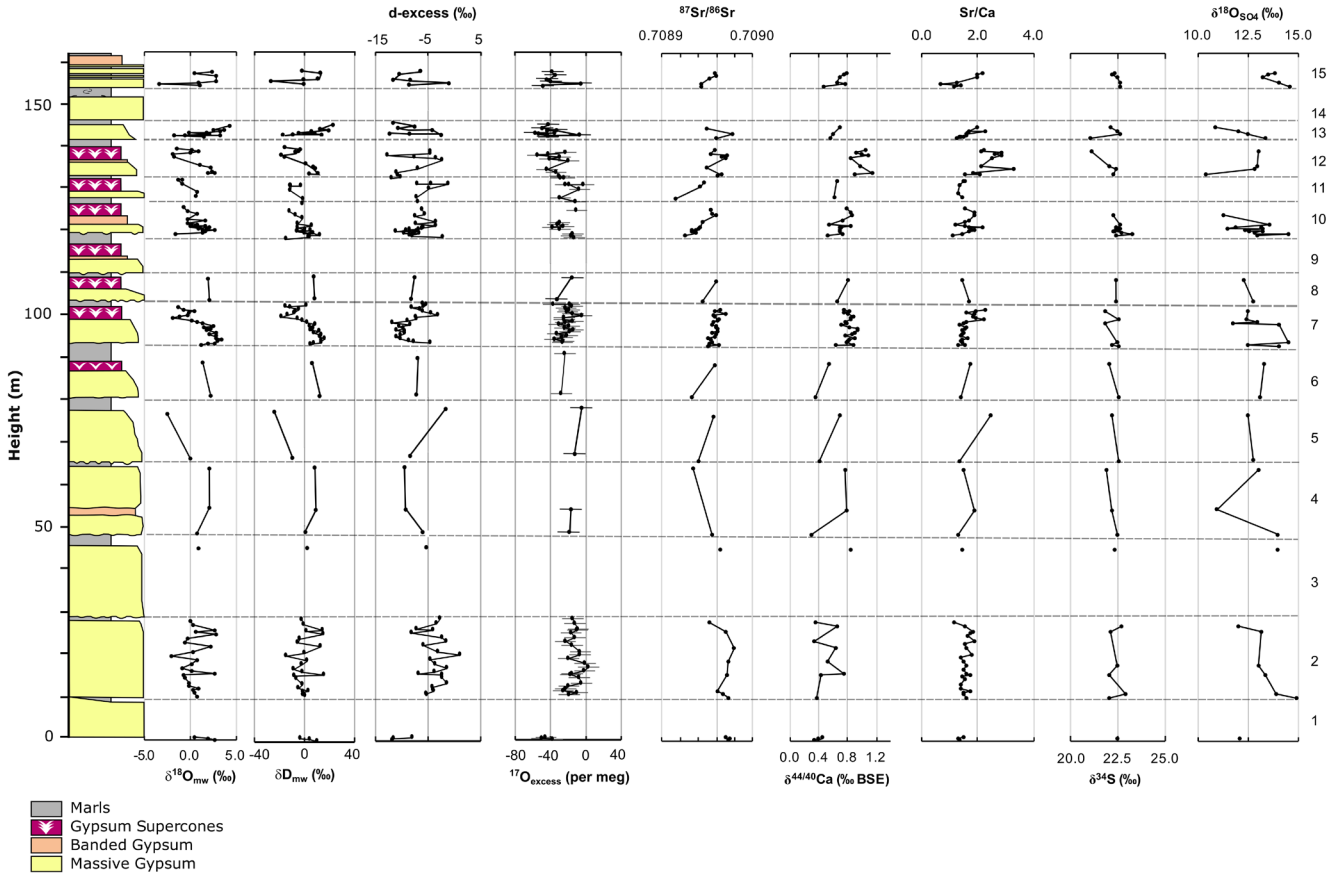

FIGURE 2 The $\delta^{18}O$, δD, d-excess and $^{17}O_{excess}$ (V-SMOW) of mother water deduced from GHW, strontium isotopes, calcium isotopes, bulk Sr/Ca ratio in gypsum, sulphur and oxygen isotopes of sulphate of individual samples are shown relative to their sample position in relation to the gypsum-marl cycles of the Yesares Member.

4.1.2 | Intra-cycle trends

Based on the oxygen and hydrogen isotope compositions of gypsum hydration water (GHW), distinct intra-cycle patterns that change progressively up-section are observed. In the lower part of the sequence (e.g., cycle 2), the $\delta^{18}O$ and δD values appear relatively homogeneous, showing no significant trend within the cycle. However, this observation is based solely on the high-resolution data available for cycle 2. The four lowermost gypsum beds consist of massive selenite with little change in crystal size, orientation, or facies variations, suggesting relatively uniform deposition.

In the case of the middle section of gypsum strata (e.g. cycles 7–12), the $\delta^{18}O$ and δD values increase upwards from the base of the section to maximum values in the gypsum palisade at ~50 to 100 cm. Importantly, the middle section coincides with the appearance of banded selenite and branching supercone structures within the cycles. Above this peak, $\delta^{18}O$ and δD fall to their lowest values at the base of the supercone structures. Isotope values in the supercones are more variable, but a small cyclic trend is apparent where the $\delta^{18}O$ and δD increase to more positive values ~150 cm above the base of the supercones and then fall to lower values at the top of the cycle. Overall, these cycles display a systematic change of increasing $\delta^{18}O$ and δD from the base of the section that reach maximum values in the lower-middle (palisade gypsum) and decrease to low isotopic values near the top (supercone).

In contrast, beginning with cycle 13 in the upper section, the cycles display upward increases in $\delta^{18}O$ and δD values from base to top (Figures 2 and 4). Cycles 13 and 15 show a general trend of higher $\delta^{18}O$ and δD values toward the top of each cycle (Figures 2 and 3). Both cycles are composed of massive, metre-thick intervals of selenite interbedded with distinct layers of carbonate marls (up to 30 cm thick) and topped by domed gypsum layers.

4.2 | Sr isotope ratios

Seventy-three gypsum samples and 12 samples from the interbedded carbonate minerals of the Messinian Yesares Member of the Sorbas Basin were processed for strontium

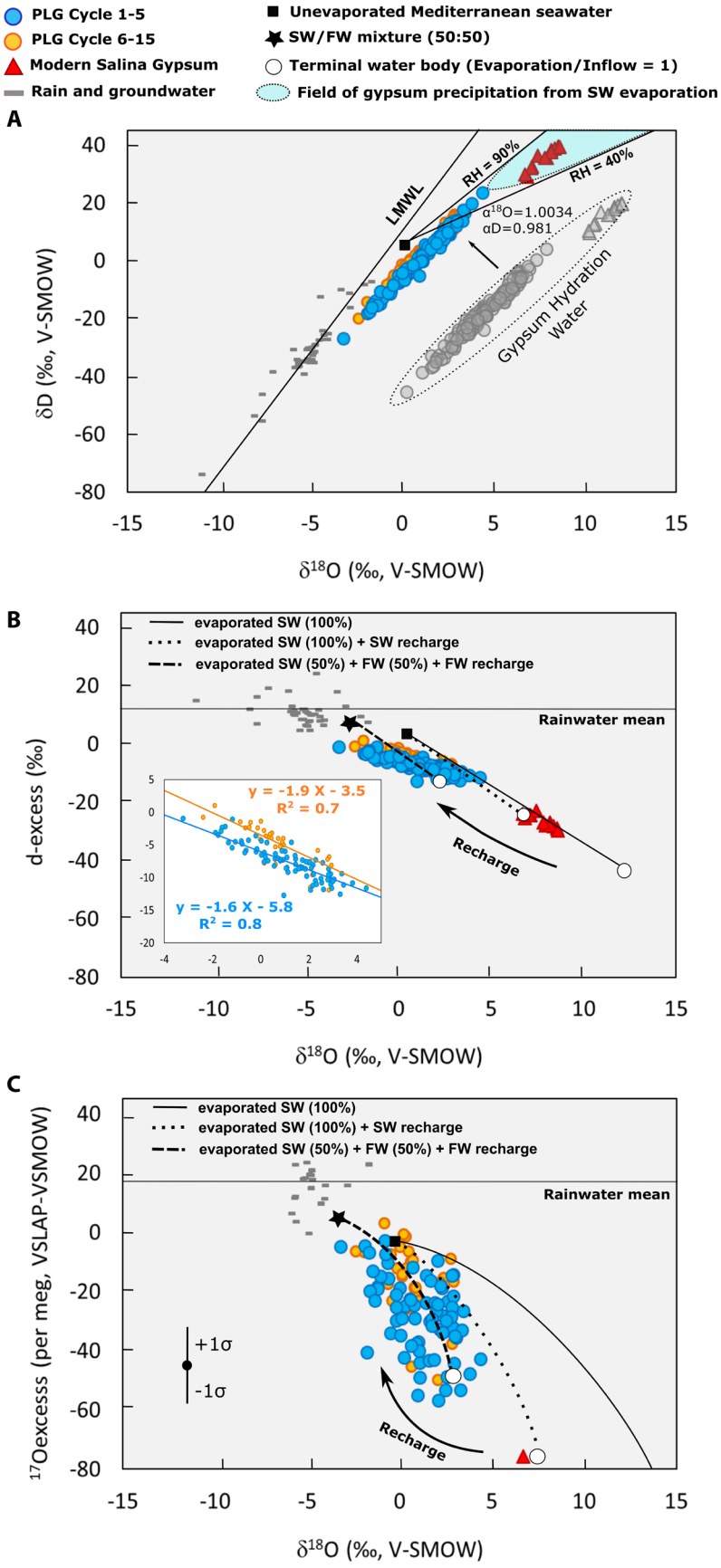

FIGURE 3 Cross plot of (A) $\delta^{18}O$ versus δD, (B) $\delta^{18}O$ versus d-excess and (C) $\delta^{18}O$ versus ^{17}O-excess of Sorbas Basin water during the formation of PLG reconstructed from stable isotope of GHW. Analytical errors (1σ) are less than the width of the symbols for $\delta^{18}O$, δD and d-excess and ± 12 for ^{17}O-excess. The isotopic composition of modern rainwaters in the Sorbas Basin (Gázquez & Calaforra, et al., 2017) and the local meteoric water line (LMWL) are given for comparison, as well as the isotopic composition of modern gypsum-forming brines in the Cabo de Gata salt factory, Almeria. We model the isotopic trajectory of evaporated water using the model described in Gázquez et al. (2018). Initial solutions with different proportions of seawater (SW) and freshwater (FW) were considered. In panel A, the trajectory of evaporated SW under different relative humidity (RH) conditions is displayed and the field where gypsum precipitation occurs (3–7 times concentrated SW). In panels B and C, the modelled the trajectory of evaporated water under RH of 60% are shown, assuming different initial solutions (100% SW and 50:50 SW/FW) and different recharge conditions, including (1) no FW or SW inputs and (2) continuous input of FW (50%) and SW (50%). Note that the data of the PLG in Sorbas match the isotopic trajectory that includes significant inputs of freshwater to the basin during gypsum formation.

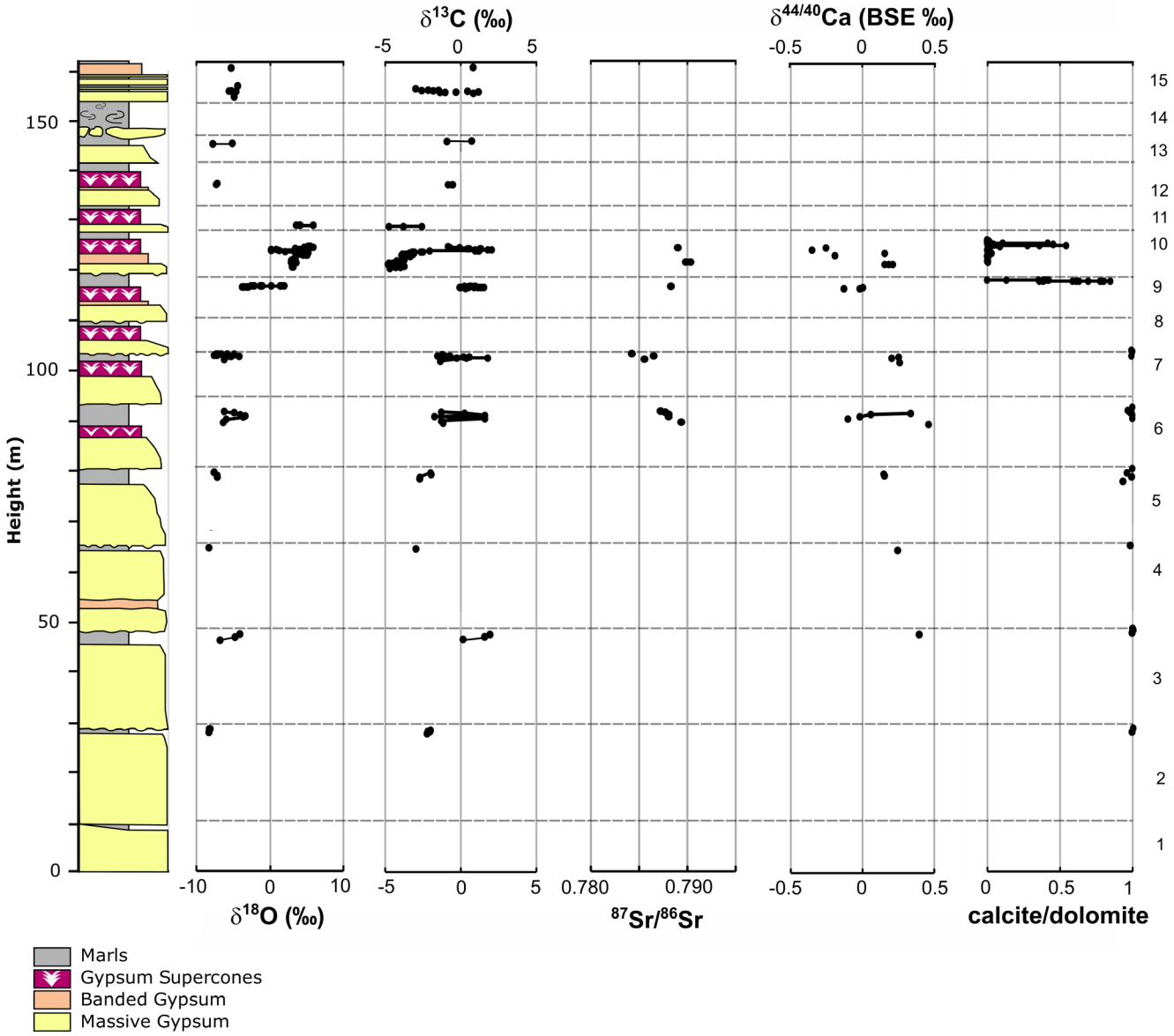

FIGURE 4 The $\delta^{18}O$ and $\delta^{13}C$ (V-PDB), strontium isotope ratio, calcium isotope ratio, and dolomite-calcite ratio of individual marl samples are shown relative to their sample position in relation to the gypsum-marl cycles of the Yesares Member.

isotopic analysis. For gypsum samples, the $^{87}Sr/^{86}Sr$ ranged between 0.708916 and 0.708979. These values fall slightly below the range of strontium isotope values expected for Messinian seawater, which varies from ~0.708989 at 5.971 Ma to ~0.709014 at 5.6 Ma relative to a NIST SRM 987 value of 0.710248 (Figure 5) (McArthur et al., 2001). In the case of the marls, the $^{87}Sr/^{86}Sr$ ranged between 0.708423 and 0.709025 (Figure 4). The $^{87}Sr/^{86}Sr$ values (and Sr content) in modern spring waters in Sierra de los Filabres were 0.708341 (0.143 ppm) and 0.708362 (0.144 ppm) for springs emanating from carbonate lithologies, whereas values were 0.718341 (0.017 ppm) and 0.713926 (0.014 ppm) for springs emanating from metamorphic schists.

4.2.1 | Inter-cycle trends

The lowermost gypsum cycle (cycle 1) has $^{87}Sr/^{86}Sr$ values that are indistinguishable from seawater (difference in mean $^{87}Sr/^{86}Sr$ from seawater = 0.000016), but the departure from global seawater values increases up-section to a maximum in cycles 10 and 11 (difference in mean $^{87}Sr/^{86}Sr$ from seawater = 0.000068). Overall, mean $^{87}Sr/^{86}Sr$ values decrease away from the seawater curve up-section, but this trend reverses at cycles 7 and 12 with a slight recovery in the direction of the global ocean seawater curve (Figure 6). Using the tuning adopted in this study, cycles 6 and 11 correspond to the low eccentricity

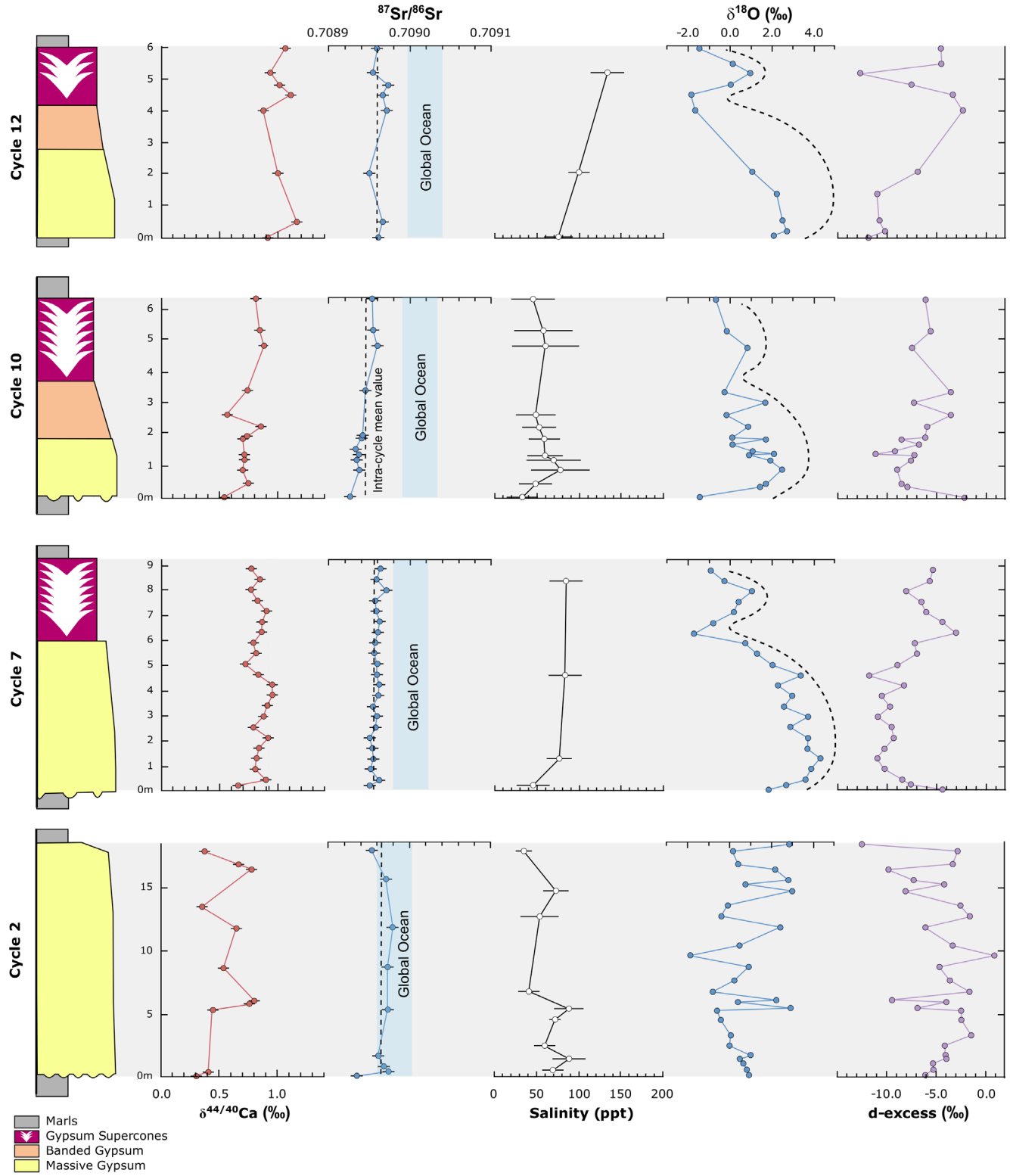

FIGURE 5 Representative examples of up-section change in isotope patterns in the lower (cycle 2) and upper (cycles 7, 10 and 12) gypsum strata, scaled to height of each of the sections. Calcium isotope data, strontium isotope data, salinity data (deduced from fluid inclusions and calculated using the equation Goldstein & Reynolds, 1994), $\delta^{18}O$ and d-excess data deduced from GHW are plotted relative to the height from which the samples were taken. Dashed lines are a guide to help visualise the trends, highlighting the similarity in $\delta^{18}O$ values in cycles 7, 10 and 12. The shaded blue areas in the strontium isotope ratio panels denotes the secular variation in the global ocean during the MSC (McArthur et al., 2001).

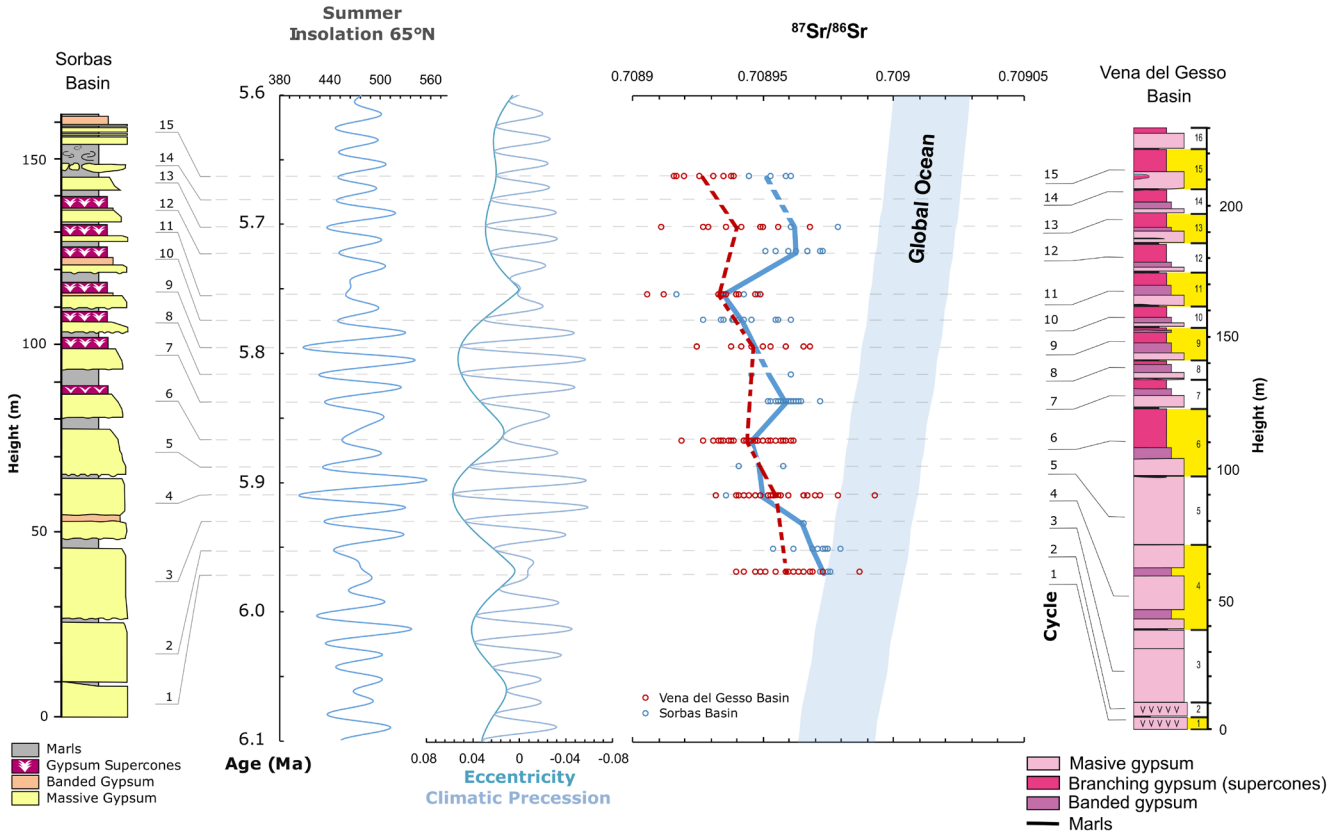

FIGURE 6 Sr isotope data of gypsum in the PLG from Vena del Gesso Basin, Northern Italy (Reghizzi et al., 2018), and the Sorbas Basin (this study) are calibrated with the orbital eccentricity and precession curves (Laskar et al., 2004). Data from the Vena del Gesso Basin show a progressive divergence from the oceanic curve upwards in the section, whereas the data from the Sorbas Basin exhibit shifts that return toward the seawater curve in PLG cycles 7 and 12. Reghizzi et al. (2018) reported data for only 7 of the 16 cycles described in the Vena del Gesso Basin, while data for 13 of the 15 gypsum beds identified in the Sorbas Basin are presented. The mean $^{87}Sr/^{86}Sr$ value for each cycle is connected by solid lines when data from two adjacent cycles are available, or by dashed lines when data from adjacent cycles are not available. The shaded blue area denotes the secular variation in the global ocean during the MSC (McArthur et al., 2001).

period, while cycles 7 and 12 are the transitions toward higher eccentricity conditions, with the $^{87}Sr/^{86}Sr$ profile defining a quasi-100 kyr cycle.

4.2.2 | Intra-cycle trends

The $^{87}Sr/^{86}Sr$ values of gypsum in cycle 2, which is considered in this study representative of the lowermost cycles of the Yesares Member, exhibit very limited intra-cycle variability and show no significant trend within individual layers (Figure 2). The mid-section cycles seem to display an increase in $^{87}Sr/^{86}Sr$ within each cycle (Figure 5); the lowest Sr isotope ratios are recorded at the base of each gypsum layer, and values increase up-section toward maximum values at the top of each cycle. This pattern is particularly evident in cycles 10 and, to a lesser extent, in cycle 7, for which high-resolution data are available (Figure 5). However, this trend is not observed in cycles 12 and 13. Additional high-resolution investigations in the remaining cycles would be necessary to confirm the consistency of these patterns. No sharp changes in the Sr isotopic composition of the gypsum are observed at the transition between gypsum facies.

The range of $^{87}Sr/^{86}Sr$ for the interbedded carbonates ($n = 9$) varies between 0.708936 and 0.708423, with an average value of 0.708720. These values are significantly lower than $^{87}Sr/^{86}Sr$ of the massive gypsum layers. The $^{87}Sr/^{86}Sr$ for the carbonate marls juxtaposed to supercones ($n = 3$) ranges from 0.709025 to 0.708991, with an average value of 0.709011, which is within the range of the Sr isotopic composition of the surrounding gypsum.

4.3 | Ca isotope ratios

The $\delta^{44/40}Ca$ values for gypsum samples ($n = 75$) range between 0.30‰ and 1.16‰ (see Table S1). The lowest $\delta^{44/40}Ca$ values are found in gypsum cycles 1 to 6, where mean ($\pm\sigma$) values of all 6 cycles are 0.53 ± 0.18‰ (Figures 2 and 5). A step change in the Ca isotopic composition of the gypsum

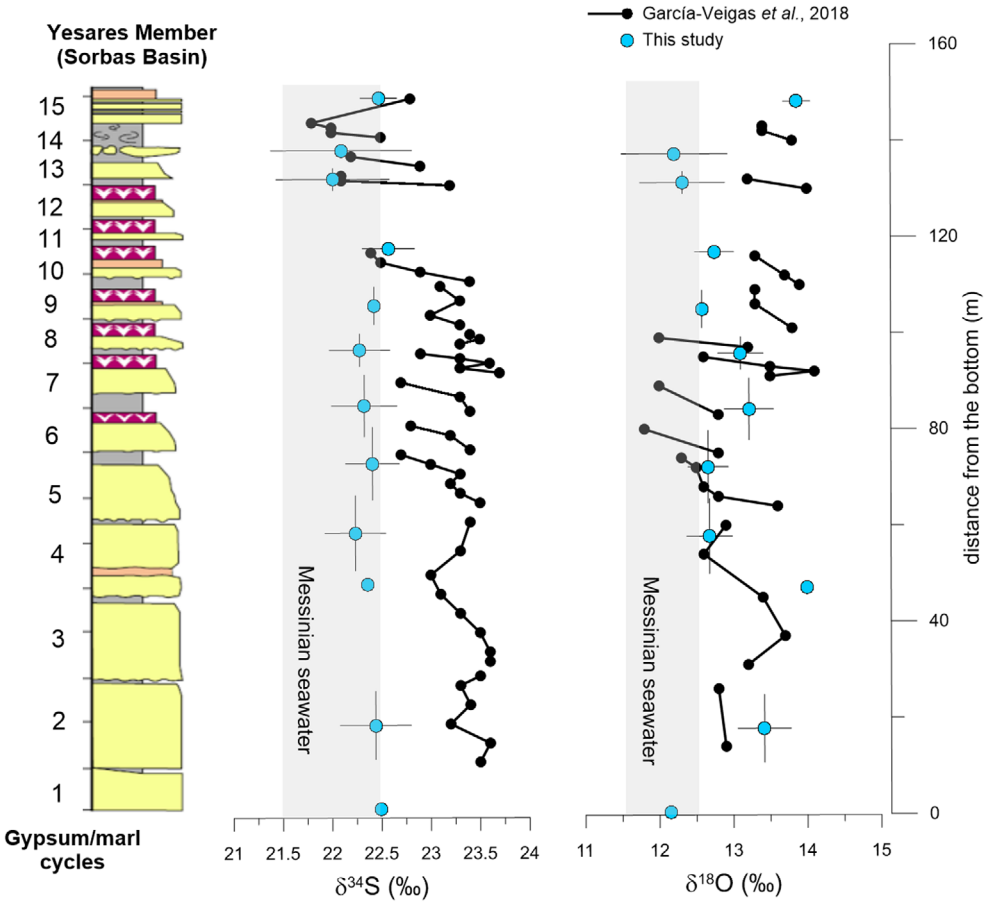

FIGURE 7 Mean intra-cycle sulphur and oxygen stable isotope values of gypsum in the PLG of the Yesares Member in the Sorbas Basin. Results from 13 gypsum bed in the Molinos sections of the Sorbas Basin reported by García-Veigas et al. (2018) are presented for comparison. Shaded grey area denotes the range of Late Miocene marine sulphates (Claypool et al., 1980).

occurs at cycle 7. Mean $\delta^{44/40}$Ca values of cycles 7 to 11 are 0.79 ± 0.10‰. Progressing up-section, Ca isotope ratios of cycle 12 also display a stepped increase compared to the lower cycles, with mean $\delta^{44/40}$Ca values of 1.01 ± 0.10‰. Calcium isotope ratios of cycles 13 to 15 (0.68 ± 0.10‰) return to similar values as cycles 7 to 11. Overall, $\delta^{44/40}$Ca values of gypsum increase up-section, with step changes defining a ~100 ka cyclicity similar to those seen in $^{87}Sr/^{86}Sr$ results (Figure 6). The range of $\delta^{44/40}$Ca for the interbedded carbonates ($n = 19$) varies between −0.35‰ and 0.46‰, and the average intra-cycle $\delta^{44/40}$Ca decreases up-section. The $\delta^{44/40}$Ca for the carbonate marls juxtaposed to supercones ranges from 0.18‰ to 0.21‰. In general, the lowest Ca isotope ratios in each cycle are observed at the base of the bed. Ca isotope ratios exhibit low-amplitude oscillations in all cycles (Figures 2 and 5).

4.4 | δ^{34}S and δ^{18}O of sulphate

Fifty-two samples were analysed for the sulphur and oxygen isotopic composition of sulphate. The δ^{34}S values of gypsum from the Sorbas Basin show a narrow range between 21.1‰ and 23.3‰ VCDT, while $\delta^{18}O_{SO_4}$ varies between 10.4‰ and 14.9‰ VSMOW. These values fall on or slightly above the range of values expected for sulphate minerals precipitated from evaporated Late Miocene seawater (i.e. $\delta^{34}S \sim 22$‰ and $\delta^{18}O_{SO_4} \sim 12$‰, relative to NBS-127 standard values of 21.1‰ and 8.6‰ for δ^{34}S and $\delta^{18}O_{SO_4}$, respectively) (Figure 7 and Figure S2).

4.4.1 | Inter-cycle trends

Gypsum δ^{34}S values remain homogenous across the entire section, with mean ($\pm\sigma$) values of 22.4 ± 0.4‰ (Figure 7 and Figure S2). The $\delta^{18}O_{SO_4}$ is also relatively unchanging across the section, displaying mean ($\pm\sigma$) values of 12.9 ± 1.0‰. From cycles 1–12, there is a slight trend toward lower $\delta^{18}O_{SO_4}$ values up-section, although cycle 15 reverses this trend and displays anomalously high values of 13.9 ± 0.5‰ (Figure 7 and Figure S2). Our δ^{34}S values are lower than García-Veigas et al. (2018) until cycle 10.

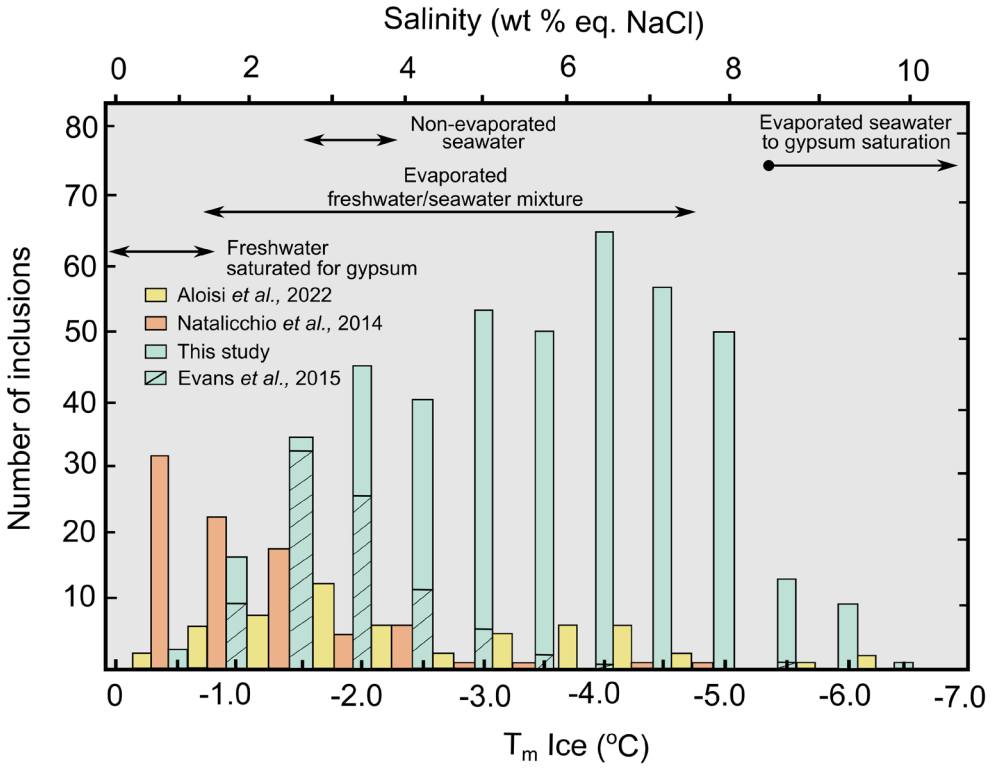

FIGURE 8 Histogram of Tm_{ice} measured in fluid inclusions of the Yesares Member of the Sorbas Basin (this study and including the results of Evans et al., 2015 from cycle 10), the Piedmont Basin PLG (NW Italy, Natalicchio et al., 2014) and the Vena del Gesso PLG (NE Italy, Aloisi et al., 2022).

4.4.2 | Intra-cycle trends

The sulphur and oxygen isotope composition of sulphate is also relatively similar within individual cycles of the Sorbas Basin (Figure 2). There are negligible differences in the isotope composition among the nucleation cone, palisade, banded selenite, and supercone facies. In cycles 4, 5, and 6, decreasing trends in $\delta^{34}S$ up-section are observed, in agreement with the observations of García-Veigas et al. (2018). This pattern is not seen in the other cycles in our dataset, which is lower resolution than the study of García-Veigas et al. (2018).

4.5 | Microthermometric analysis

Thirty-four samples from the Messinian gypsum of the Sorbas Basin and 2 samples from the modern Salina at Cabo de Gata, Almería, Spain, were selected for microthermometric analysis (see Table S1). The final melting temperature (Tm_{ice}) of 205 primary Messinian inclusions ranged between −0.2°C and −6.1°C, with an average Tm_{ice} of −3.2°C (Figure 8). Using the revised equation and table for determining the freezing point depression of H_2O–NaCl solutions of Bodnar (1993), average salinity estimates of individual samples range from 2.9% to 8.5% (average 5.3 wt% NaCl equivalent). Tm_{ice} of modern gypsum from the Cabo de Gata Salina ranged between −6.5°C and −10.1°C (average −8.0°C), corresponding to an average salinity of 11.7%. Within the section, the average wt% NaCl equivalent of gypsum from cycles 1 to 9 is 5.1% ± 1.1% (Figure 5). These values are well below the threshold for gypsum precipitation from the evaporation of seawater alone. The mean wt% NaCl of cycle 11 is 7.2% ± 1.2%, representing a significant increase compared to the lower cycles.

4.6 | XRD, wt% calcite and wt% dolomite of bulk carbonates

A hundred and six marl samples were analysed by XRD (see Table S1). The results are semiquantitative and indicative of the relative abundances of common mineralogical components only. In addition to clay, the major phases are gypsum, calcite, and dolomite. The marls interbedded with the lower 7 cycles contain predominantly calcite. The marls at the base of cycle 10 contain both calcite and dolomite (Figure 9). The ratio of dolomite-to-calcite in the lower marls of cycle 10 increases up-section such that dolomite becomes more dominant toward the gypsum–marl contact. Fine-grained gypsum

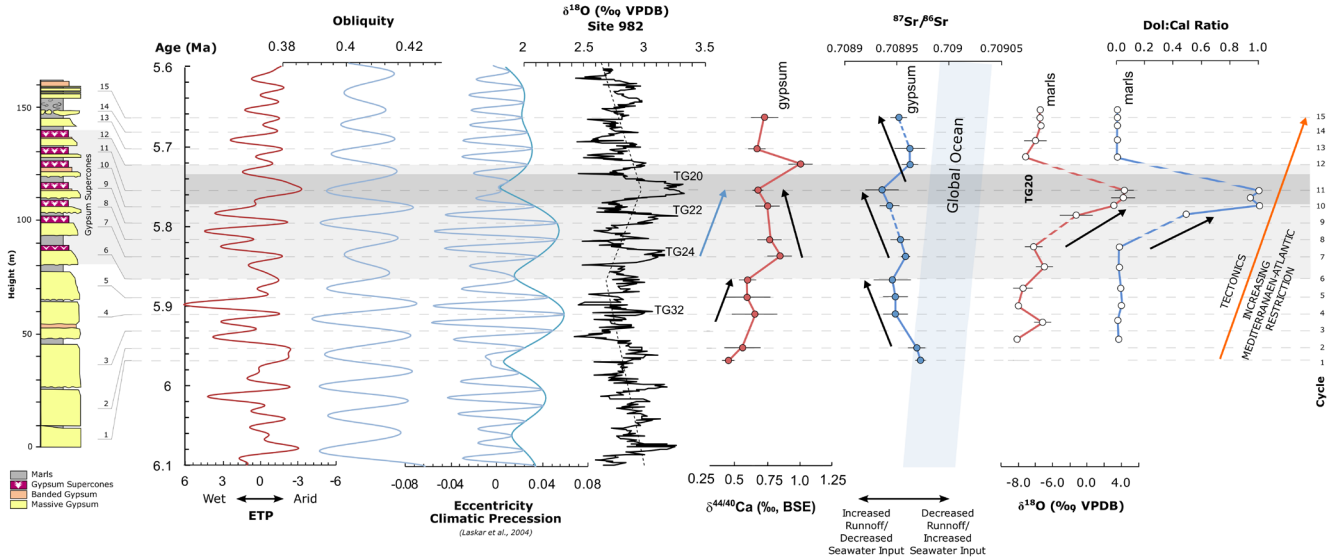

FIGURE 9 Mean inter-cycle $^{87}Sr/^{86}Sr$ data and $\delta^{40/44}Ca$ data from gypsum beds and $\delta^{18}O_{carb}$ and dolomite-calcite ratio of the interbedded carbonates are plotted against their designated cycle. Error bars define $\pm 1\sigma$ of the data in each cycle. The mean value for each cycle is connected by solid lines when data from two adjacent cycles are available, or by dashed lines when data from adjacent cycles are unavailable. Note that carbonate data plotted between the horizontal dashed lines denote carbonate samples located between gypsum beds, whereas carbonate samples associated with supercones lie on the dash line. Each gypsum bed of the Yesares Member is plotted in relation to its proposed orbital forcing (Laskar et al., 2004), where gypsum precipitation correlates with insolation minima. The benthic $\delta^{18}O$ of Site 982 (Hodell et al., 2001; modified by Drury et al., 2018) is also shown, and the major glacial stages are indicated. The light grey horizontal grey band indicates the appearance of supercones in the sequence (cycles 6–12). The dark grey horizontal band highlights the glacial Stage TG20. The blue arrow highlights the period of progressive cooling and global sea-level lowering through Stages TG24, TG22 and TG20. The orange arrow indicates the expected, gradual influence of the tectonic restriction of the Mediterranean-Atlantic exchange of the isotope systems shown. The black arrows highlight key trends in $^{87}Sr/^{86}Sr$, $\delta^{44/40}Ca$, $\delta^{18}O_{carb}$ and dolomite-calcite data. Note that there is significant correlation between shifts in $^{87}Sr/^{86}Sr$, $\delta^{44/40}Ca$, $\delta^{18}O_{carb}$ and dolomite-calcite data and glacial Stages TG24, TG22 and TG20. Eccentricity, Tilt and Precession (ETP) is calculated from orbital solutions (Laskar et al., 2004).

within the marl is abundant in the upper marl from 8 cm below the marl-gypsum contact. Between cycles 10 and 11, marls are predominantly composed of dolomite with minor amounts of calcite. Marls juxtaposed to supercones in cycles 10 and 11 are purely dolomitic and contain varying proportions of gypsum. The mineralogy shifts back to calcite beginning with cycle 12.

4.7 | $\delta^{18}O_{carb}$ and $\delta^{13}C$ of bulk carbonates

The oxygen and carbon isotope composition of 138 carbonate samples varies from −8.3‰ to 5.8‰ for $\delta^{18}O_{carb}$ and from −4.9‰ to 2.0‰ for $\delta^{13}C$ (Figure S3). The carbon and oxygen isotope composition of the carbonate rocks is within the range of other Messinian carbonates associated with evaporite deposits in the Mediterranean (Longinelli, 1979). The $\delta^{18}O_{carb}$ of the marls from cycles 1–7 averages -6.1 ± 1.4‰, whereas the $\delta^{13}C$ averages -0.8 ± 1.4‰ (Figure 10). At the base of cycle 10, mean ($\pm\sigma$) $\delta^{18}O_{carb}$ and $\delta^{13}C$ increase to -1.2 ± 1.9‰ and 0.6 ± 1.9‰, respectively. Marls juxtaposed to supercones in cycles 10 and 11 show the highest $\delta^{18}O_{carb}$ values, but the lowest $\delta^{13}C$ values, averaging 3.1 ± 0.2‰ and -4.4 ± 0.4‰, respectively. Additionally, the marls between cycle 10 and 11 show high $\delta^{18}O_{carb}$ and low $\delta^{13}C$ values, averaging 4.1 ± 1.4‰ and -1.6 ± 2.1‰, respectively. In this cycle, negative excursions in the $\delta^{18}O_{carb}$ are well correlated with a decrease in the calcite:dolomite ratio. Above cycle 12, the $\delta^{18}O_{carb}$ and $\delta^{13}C$ return to values similar to those of cycles 1–7, averaging −5.8‰ and −1.1‰, respectively.

5 | DISCUSSION

The conditions, causes, and mechanisms leading to the deposition of the PLG remain controversial (Bigi et al., 2022; Aloisi et al., 2022; Ryan & Raad, 2025). What was the composition and salinity of the brines that formed the gypsum and carbonate layers? Did they form from evaporated seawater or a hybrid brine consisting of a mixture of seawater and freshwater? What were the relative roles of tectonics, affecting Mediterranean–Atlantic exchange and glacio-eustatic sea-level variability, and orbital forcing on evaporite deposition? A multi-isotope

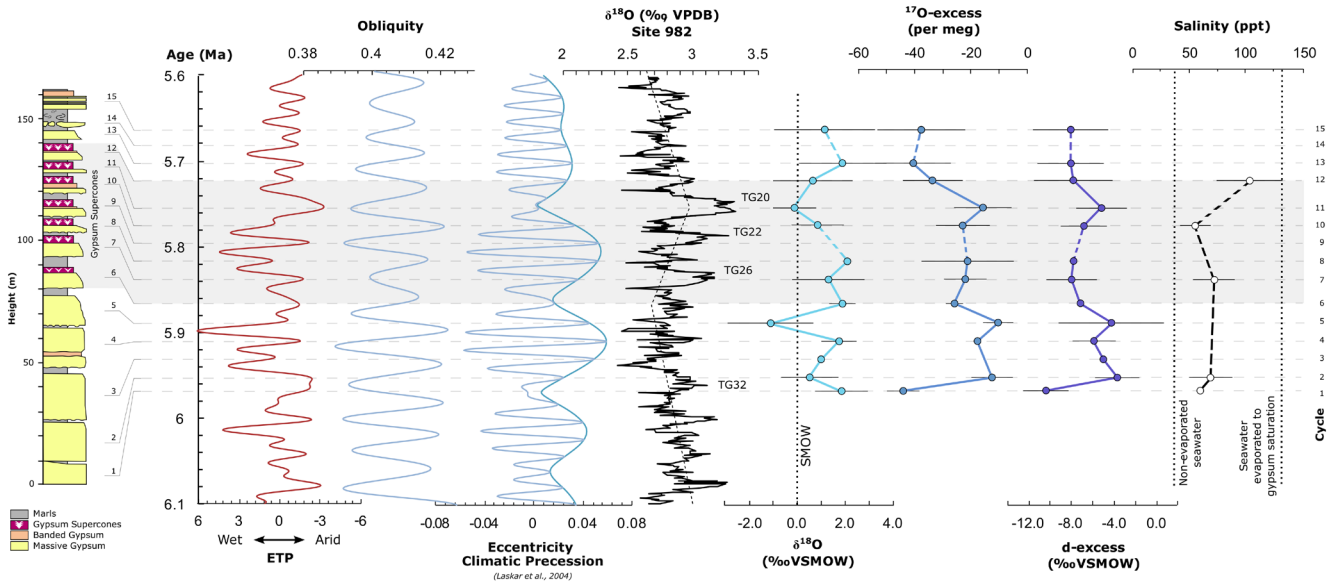

FIGURE 10 Mean inter-cycle $\delta^{18}O$, ^{17}O-excess and d-excess data (calculated from measurement of GHW) and salinity data (deduced from fluid inclusions and calculated using the equation of Goldstein & Reynolds, 1994) are plotted against their designated cycle. The mean value for each cycle is connected by solid lines when data from two adjacent cycles are available, or by dashed lines when data from adjacent cycles are not available. Error bars define $\pm 1\sigma$ of the data in each cycle. Each gypsum bed of the Yesares Member is correlated to its presumed orbital forcing (Laskar et al., 2004), where gypsum precipitation correlates with insolation minima. The benthic $\delta^{18}O$ of Site 982 (Hodell et al., 2001; modified by Drury et al., 2018) is also shown and the major glacial stages are indicated. The horizontal grey band indicates the occurrence of gypsum supercones in cycles 6–12. Eccentricity, Tilt and Precession (ETP) is calculated from orbital solutions (Laskar et al., 2004).

approach is used to explore these outstanding questions related to PLG formation and propose a scenario to reconcile the various geochemical data.

5.1 | Brine composition during PLG deposition

The commonly accepted mechanism for the formation of the PLG is the gypsum precipitated from the evaporation and concentration of seawater formed by continuous inflow from the Atlantic Ocean, providing the necessary ion supply (Krijgsman & Meijer, 2008; Topper & Meijer, 2013). Water isotope ratios of GHW (Aloisi et al., 2022; Evans et al., 2015) and salinities determined from fluid inclusions (e.g. Natalicchio et al., 2014) suggest that gypsum precipitation may have occurred at salinities lower than those expected for the evaporation of seawater to gypsum saturation (~130 g L^{-1}). This has given rise to "the geochemical riddle of low-salinity gypsum" (Aloisi et al., 2022).

The variation in $\delta^{18}O$, $\delta^{17}O$, and δD values of the water from which the PLG formed in the Sorbas Basin is relatively low, ranging from −1.7‰ to 2.3‰, −3.2‰ to 4.4‰, and −26.8‰ to 23.5‰, respectively. If the Yesares gypsum formed directly from the evaporation of seawater, the expected isotope composition would be significantly higher than those measured and probably closer to the values of gypsum formed today at the Salinas of Cabo de Gata, Almeria (Figure 3). Additionally, microthermometric salinity data indicate that Messinian fluid inclusions do not have salinities high enough to fall within the range of gypsum saturation if derived from seawater evaporation alone (Figure 8). Bigi et al. (2022) interpreted the low salinity of fluid inclusions as resulting from post-depositional processes (crack and seal), but this interpretation has been challenged by Aloisi et al. (2022), who concluded that the fluid inclusion salinity and isotopic data of gypsum hydration water represent a primary signal. They suggested that the method used by Bigi et al. (2022) for the thermometric analyses (i.e., fast heating of the gypsum samples from −100 to 120°C to promote nucleation of bubbles within the fluid inclusion) can alter the volume of the inclusion and produce water diffusion, thereby affecting the estimations of water salinity. Additional evidence for the relatively low salinity of gypsum precipitation in the Sorbas Basin during the MSC is supported by the presence of centric diatoms, such as the *Thalassiosiraceae* genus, found within gypsum crystals of the lowest gypsum cycles of the Yesares Membrer (Pellegrino et al., 2021). These diatoms preferentially thrive in marine to brackish waters and do not tolerate hypersaline conditions, even when salinity is well below the gypsum precipitation threshold.

Comparison of the isotopic composition (i.e., $\delta^{18}O$ vs. d-excess and $\delta^{18}O$ vs. ^{17}O-excess) of the Sorbas Basin water during the Messinian with isotope mass-balance modelling of evaporation trajectories (Figure 3) suggests that our results cannot be explained by the simple evaporation of a seawater–freshwater mixture in a closed basin, where evaporating water evolves along a trajectory toward an isotopic end-point (Surma et al., 2018). Basin recharge (mixing) drives the water's isotopic composition along a trajectory below the expected evaporation trend (Figure 3), especially when considering ^{17}O-excess vs. $\delta^{18}O$, as has been demonstrated in other modern hydrologic systems (Herwartz et al., 2017; Surma et al., 2018; Voigt et al., 2021). Basin recharge by meteoric water is the only mechanism that can produce the observed water isotope trends for the Sorbas Basin PLG, suggesting that gypsum formed at a steady state with continuous inflow of freshwater. Other authors have reached the same conclusion for PLG deposits elsewhere (e.g., Caltanisseta Basin, Sicily; Vena del Gesso and Piedemont Basins; Aloisi et al., 2022), northern Apennines and Polemi Basin, Cyprus (Deuβen et al., 2024), suggesting that similar hydrologic dynamics may have operated in marginal basins throughout the wider Mediterranean Sea during the first stage of the MSC.

The significant freshwater contribution to the mother brines recorded by GHW and salinity deduced from fluid inclusions is supported by strontium isotope data obtained from the same samples. Our results from the PLG of the Sorbas Basin show that $^{87}Sr/^{86}Sr$ values are significantly lower than global seawater values, with an increasing departure from global ocean $^{87}Sr/^{86}Sr$ values up-section (Figure 6). These findings contrast with some earlier studies which concluded that the near-oceanic $^{87}Sr/^{86}Sr$ values suggested the PLG precipitated dominantly from seawater (e.g. Flecker et al., 2002; Flecker & Ellam, 2006; Lu & Meyers, 2003; Lugli et al., 2007). Topper and Meijer (2013) demonstrated that when Mediterranean river discharge and meteoric inputs constitute around 40% of the water fluxes, the $^{87}Sr/^{86}Sr$ value of the basin will deviate measurably from the Messinian seawater value (~0.70900) toward lower riverine values of the Rhone (~0.70872) and the Nile (~0.70600) (Flecker & Ellam, 2006).

Our strontium isotope measurements from headwater rivers in the Sierra de los Filabres, northwest of the Sorbas Basin, yield $^{87}Sr/^{86}Sr$ values of approximately 0.7083 for carbonate spring water ($n = 2$) and much higher values of up to 0.7183 for spring water in contact with schist ($n = 2$). Importantly, the carbonate aquifer water has significantly higher Sr (~0.14 ppm) than that of the schist aquifer (~0.016 ppm), reflecting the higher Sr concentrations and increased susceptibility of carbonates to chemical weathering. Similar trends are observed in global riverine data that show an inverse relationship between Sr concentration and $^{87}Sr/^{86}Sr$ values (Palmer & Edmond, 1992). This indicates that any contribution from rivers draining carbonate or evaporite lithologies will have a much greater effect on the Sr isotope mass balance of the basin hydrology than will rivers draining metamorphic terrains. Thus, we hypothesise that riverine contributions to the Sorbas Basin may have had lowered the $^{87}Sr/^{86}Sr$ values of water compared to seawater. The $^{87}Sr/^{86}Sr$ values of the springs weathering carbonates are comparable to the lowest $^{87}Sr/^{86}Sr$ ratios observed in some marl beds (~0.7084) and in the PLG gypsum (~0.7089).

Previous studies of foraminifera in the Sorbas Basin suggested that riverine strontium input to the basin had $^{87}Sr/^{86}Sr$ values (~0.7091) higher than those of the global Messinian Ocean (Modestou et al., 2017), but this is not supported by our measurements of modern spring waters. The progressive decrease of $^{87}Sr/^{86}Sr$ up-section in the Yesares Member and departure from global ocean $^{87}Sr/^{86}Sr$ values indicate a gradual reduction of marine inflow and the increasing influence of continental input (Figure 6). A simple model by Ryan and Raad (2025) with unidirectional inflow or outflow and evaporation controlled by ion activity ratio and forced by eccentricity-modulated precession cycles reproduces the decreasing trend in $^{87}Sr/^{86}Sr$ ratios observed in the PLG of Sorbas (this study) and Vena del Gesso Basin (Reghizzi et al., 2018). Our data indicate that this trend is produced by a reduction of periodic marine inflow relative to a constant supply of river water.

The high proportion of freshwater inflow into the Mediterranean combined with surface evaporation produced a brine that flowed toward the deeper parts of the basin, resulting in significant basin stratification (Simon & Meijer, 2017). Indeed, the higher-than-expected $\delta^{34}S$ and $\delta^{18}O_{SO_4}$ values for Late Miocene seawater ($\delta^{34}S \sim 21‰$; $\delta^{18}O_{SO_4} \sim 12‰$) of gypsum of both the Yesares Member of Southern Spain ($21.1‰ < \delta^{34}S < 23.3‰$; $10.4‰ < \delta^{18}O_{SO_4} < 14.9‰$) and Caltanissetta Basin of Sicily ($22.4‰ < \delta^{34}S < 23.2‰$; $12.7‰ < \delta^{18}O_{SO_4} < 14.6‰$) were likely caused by cyclic microbial sulphate reduction in a stratified water column (De Lange & Krijgsman, 2010; García-Veigas et al., 2018). Our $\delta^{34}S$ and $\delta^{18}O_{SO_4}$ values and trends differ compared to those of García-Veigas et al. (2018), who collected their samples from 13 gypsum beds from the Molinos section of the Sorbas Basin. It is possible that slightly different environments existed during gypsum deposition, leading to different redox processes and resulting in distinct sulphur and oxygen isotopic signatures in the sulphate. Aloisi et al. (2022) suggested that reduced sulphur compounds (S^0) were deposited in the deepest part of the Mediterranean marginal basin during periods of water column stratification (i.e., relatively wetter periods). Subsequently, efficient oxidation of reduced

sulphur to SO_4^{2-} occurred because of oxygenation of the basin bottom during water column mixing events under arid climate conditions. Additional $\delta^{34}S$ and $\delta^{18}O_{SO_4}$ results are needed to demonstrate if there are isotopic gradients in gypsum deposits throughout the basin.

5.2 | Tectonic, orbital and glacio-eustatic control on basin hydrology

5.2.1 | Tectonic control of basin hydrology

Tectonic restriction of the Mediterranean basin acted on longer timescales than orbital and glacio-eustatic processes and is responsible for the general long-term trends up-section in many parameters, including gypsum bed thickness, decreased strontium isotopes, increased calcium isotopes, decreased d-excess and ^{17}O-excess of gypsum hydration water. Do Couto et al. (2014) suggested that the formation of the Sorbas Basin started with extensional tectonics that preceded basin shortening and inversion around 8 Ma. The basin functioned as an active depocenter, locally exceeding 2 km in depth with a distinctly asymmetric bathymetric profile (Do Couto et al., 2014). Localised subsidence took place between 7.6 Ma and 6.5 Ma during the deposition of the pre-Messinian Azagador Member and the early Messinian Abad Marl Unit. Subsequently, basin shallowing occurred due to sediment infilling between 6.5 Ma and 6.0 Ma. The basin bathymetry appears to have remained comparatively more stable between 6.0 Ma and 5.6 Ma when the PLG was deposited, although uplift continued through this period. The current elevation of the Sorbas Basin, exceeding 450 m a.s.l. in some areas, cannot be attributed solely to glacio-eustatic changes and necessarily involves tectonic uplift of the basin. Indeed, Sierra de Cabrera, located only 5 km southeast of the Sorbas Basin, considered the youngest mountain range on the Iberian Peninsula, began to emerge around 5.5 million years ago during the Messinian, with uplift continuing throughout the Plio-Pleistocene (Valetti et al., 2019).

The intra-cycle isotopic profiles and changes in gypsum and clay bed thickness observed in the Sorbas section can be explained by the influence of variable Mediterranean–Atlantic exchange and the effect of ion activity on evaporation (Ryan & Raad, 2025). The lower 5 gypsum cycles are massive, with relatively homogenous isotopic profiles, reflecting deposition under conditions of hydrological stability and relatively deep water. Above cycle 5, the gypsum beds thin and clay layers thicken, likely indicating a shallowing of the water in the basin. Our data show that there is also more variation in the geochemical data of the gypsum beds in the upper cycles. The rate of gypsum accumulation decreased over time due to a decline in water activity as salinity increased and ocean inflow diminished. The evaporative model proposed by Ryan and Raad (2025) supports this interpretation, showing a reduction in Atlantic–Mediterranean exchange that aligns with the progressively thinner PLG beds observed above PLG bed 6. Thus, the reduction in gypsum bed thickness up-section is attributed to a decrease in seawater input to the basin caused by tectonic activity that locally restricted the sill depth, as evidenced by the uplift of the Sierra de Cabrera Mountain range (Valetti et al., 2019). However, a similar change in gypsum strata thickness is also seen across the Northern and Central Apennines (Lugli et al., 2010), suggesting that the mechanisms involved may have been regional (i.e. gradually constricting of the Mediterranean–Atlantic gateways; Simon et al., 2017; Krijgsman et al., 2018). Progressive basin restriction during PLG deposition in the Sorbas Basin is further supported by the gradual up-section increase in $\delta^{44/40}Ca$ values in the gypsum (Figure 11). This trend can be explained by the preferential incorporation of the lighter calcium isotope (^{40}Ca) into gypsum, as calcium isotope fractionation for gypsum is less than unity (Harouaka et al., 2014). This "prior gypsum precipitation" leads to an enrichment of the residual brine in the heavier isotope (^{44}Ca) and consequently, to higher $\delta^{44/40}Ca$ values in gypsum up-section, as demonstrated by modelling conducted by Harouaka et al. (2014). Interestingly, the $\delta^{44/40}Ca$ in the interbedded marls decrease up-section from cycle 2 to 11, resulting in a divergent trend with respect to gypsum. The shift to lower $\delta^{44/40}Ca$ values in the marls could potentially be attributed to increased rates of carbonate mineral precipitation upsection. Faster rates of carbonate mineral precipitation lead to greater kinetic calcium isotope fractionation, resulting in an enrichment of ^{40}Ca in the mineral phase (AlKhatib & Eisenhauer, 2017; Nielsen et al., 2012); if these are volumetrically significant, they can contribute to the enrichment of the residual brine in the heavier isotope (^{44}Ca). One possibility is the recent observation of a strong calcium isotope fractionation during pure culture experiments involving sulphate reducing bacteria where carbonate minerals form through microbially induced mineralization (Bradbury et al., 2020). Evans et al. (2015) previously highlighted evidence of microbially mediated carbonate in cycle 10 of the Yesares Member; therefore, if the marls include volumetrically significant amounts of microbially mediated carbonate minerals, these could contribute to lower overall $\delta^{44/40}Ca$ measured in the carbonate fraction. Importantly, a purely tectonic driving mechanism would result in a unidirectional trend in the facies and geochemical profile, reflecting uplift. But minor reversals in geochemical variations of the Sorbas Basin are observed, suggesting additional processes were involved.

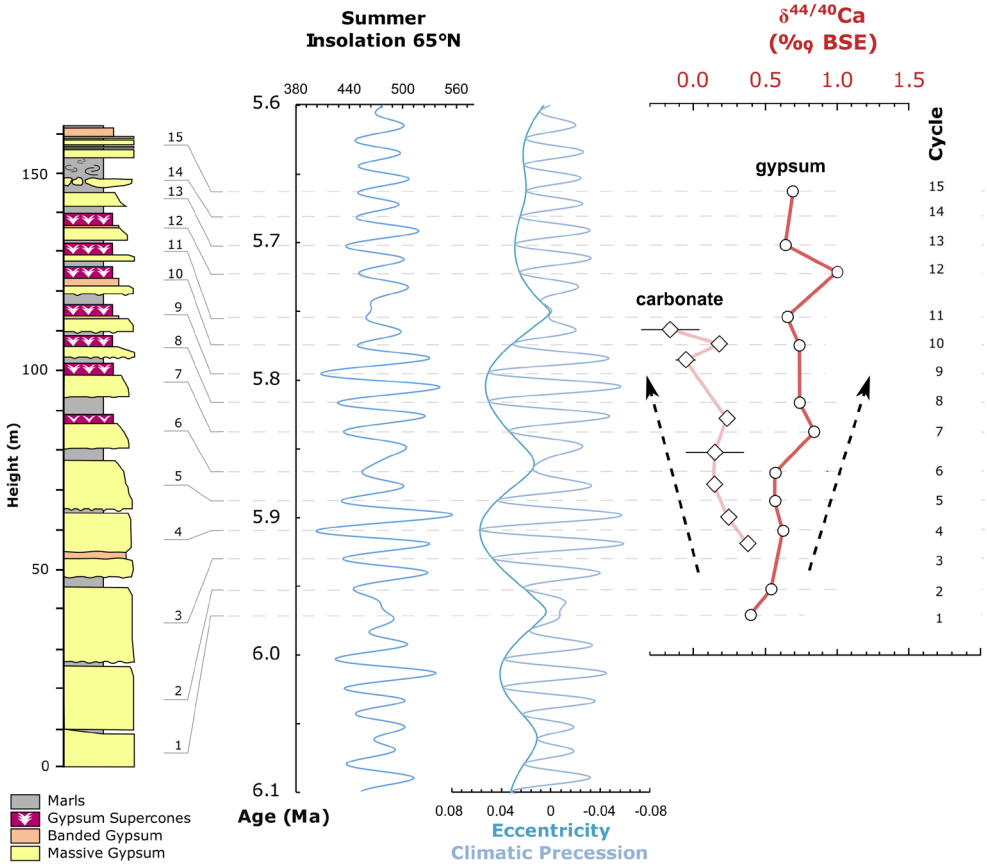

FIGURE 11 Mean inter-cycle $\delta^{44/40}$Ca data of the gypsum and interbedded carbonate minerals are plotted against their designated cycle. Error bars define $\pm 1\sigma$ of the data in each cycle. Note that carbonate data plotted between the horizontal dashed lines denote carbonate samples located between gypsum beds, whereas carbonate samples associated with supercones lie on the dash line. Note the relative difference in gypsum and carbonate $\delta^{44/40}$Ca (grey area) increases up-section.

5.2.2 | Orbital control of basin hydrology

Gypsum-marl cycles of the PLG are interpreted to reflect precession cycles, with gypsum precipitated at the precession maxima (i.e. minimum summer insolation when summer solstice coincided with aphelion) when evaporation exceeded precipitation and marls were deposited during precession minima (maximum summer insolation when summer solstice and perihelion coincided) when rainfall increased (Krijgsman et al., 1999, 2001). Within a depositional cycle, variations in oxygen and hydrogen isotopes of GHW (Evans et al., 2015) and $^{87}Sr/^{86}Sr$ (e.g. Flecker & Ellam, 2006; Lugli et al., 2010; Reghizzi et al., 2018; Topper et al., 2014) support changing freshwater input forced by orbital precession. Eccentricity strongly modulated the amplitude of the precession cycle, and obliquity played a secondary role depending upon its phasing with precession.

The $^{87}Sr/^{86}Sr$ results of the carbonate marls are always lower than that of the interbedded gypsum layers. This agrees with Sr isotope analysis of mollusc shells that generally yield $^{87}Sr/^{86}Sr$ values equal to or lower than that of gypsum measured in the same section (Reghizzi et al., 2018). Lower $^{87}Sr/^{86}Sr$ in marls suggests increased supply of riverine inputs to the Sorbas Basin during periods of precession minimum. The low $^{87}Sr/^{86}Sr$ values of 0.7083 for carbonate springs in the surroundings of the Sorbas Basin support this interpretation. In addition, the weathering of earlier marls from the Yesares Formation or marls from the pre-MSC Abad Formation may have also influenced the strontium isotope composition of carbonates formed during the later stages of the MSC.

During the climatic transition from a precession minimum to maximum, river input is expected to decrease while evaporation/inflow to the basin increases, leading to the precipitation of gypsum beds. Evans et al. (2015) showed that, in a single cycle (cycle 10), the $\delta^{18}O$ and δD of GHW increased from low values at the base of the cycle to a maximum in the massive gypsum palisade and decreased again to lower values in the supercones at the top of the cycle. This pattern, together with changes in mineralogy in the carbonate minerals at the base of the cycle (calcite–dolomite–gypsum), is consistent with a precession-driven change in climate. In the present study,

this pattern has been reproduced in cycles 7, 11, and 12, at the Covadura Cave, Río de Aguas and Barranco del Infierno sections, respectively (Figure 2). Remarkably, this sinusoidal intra-cycle trend may begin from the first occurrence of branching supercones in cycle 6, although this cycle has not been sampled with high resolution.

Strontium concentrations (e.g. Rosell et al., 1998) and salinity deduced from fluid inclusions in gypsum (Figure 5) also show relatively uniform values in the lower beds (i.e. cycles 1–4) but become more variable with the sixth gypsum cycle and above. Importantly, our measurements of fluid inclusion in cycle 12 gypsum indicate higher water salinity (i.e. 7.2 ± 1.3 wt% NaCl) compared to lower cycles (e.g. 4.4 ± 0.8 wt% NaCl in cycle 10 and 5.8 ± 1.1 wt% NaCl in cycle 2) (Figure 9). Increasing salinity during the formation of the PLG is also supported by the results of the evaporative modelling conducted by Ryan and Raad (2025). These authors suggested that the activity coefficient of gypsum decreased as water salinity increased, due to a reduction in ocean inflow into the Mediterranean. This led to lower gypsum saturation starting from cycle 6, resulting in thinner PLG beds higher in the section. Taken together, our results and the modelling by Ryan and Raad (2025) suggest that salinity during the formation of the upper gypsum cycles was likely driven by increasing basin restriction and a higher evaporation-to-inflow ratio, even though seawater input into the basin diminished during these later stages of PLG formation.

Sulphur isotopes become more variable beginning with cycle 5 and show a decrease through each cycle (Figure 7; García-Veigas et al., 2018), although these trends are not apparent in our $\delta^{34}S$ data perhaps owing to a lower sampling interval. The $\delta^{44/40}Ca$ and $^{87}Sr/^{86}Sr$ values obtained from the PLG also display trends in the upper part of the section beginning with cycle 6 (Figures 9 and 11). The lowest $\delta^{44/40}Ca$ and $^{87}Sr/^{86}Sr$ values are usually found at the base of each gypsum bed, although the variability of both $\delta^{44/40}Ca$ and $^{87}Sr/^{86}Sr$ within each cycle is low (Figure 5). Importantly, there is no significant relationship between $\delta^{44/40}Ca$ and crystal size and thus the growth kinetics are unlikely to be the main controlling factor of $\delta^{44/40}Ca$ in the selenitic gypsum facies.

Isotope ratios of oxygen and hydrogen measured in GHW are relatively high in the massive selenite at the base of the gypsum cycles and fall toward lower values in the supercone structures. This indicates that the freshwater-dominated fluid that formed the massive gypsum at the base of each cycle required relatively high levels of evaporation to reach gypsum saturation, resulting in increased $\delta^{17}O$, $\delta^{18}O$, and δD values. The supercone structures likely formed from fluids that were composed of less meteoric input compared to the base of the cycle, but were more enriched in calcium and sulphate ions, requiring less evaporation to reach gypsum saturation. The necessary ionic input may have resulted either from the weathering of evaporites and marls from previous cycles or from calcium introduced into the basin by rivers that had previously dissolved carbonate rocks (Evans et al., 2015; Rossi et al., 2015). The relatively high concentration of Ca^{2+} in spring (up to 40 ppm in our measurements of headwater in Sierra de los Filabres) allows us to hypothesise that, during wetter periods, increased spring discharge into the Sorbas Basin may have contributed to a higher Ca^{2+}/SO_4^{2-} ratio, leading to gypsum supersaturation.

In contrast, there are no significant intra-cycle trends in $\delta^{44/40}Ca$ and $^{87}Sr/^{86}Sr$ values in the lower gypsum beds (i.e., cycles 1–5), resulting in a weak correlation between $\delta^{44/40}Ca$ and $^{87}Sr/^{86}Sr$ within each cycle (Figure S4). This lack of correlation suggests that the slight increase in $\delta^{44/40}Ca$ from the base to the top of individual cycles could reflect ongoing Rayleigh fractionation in the brine during gypsum precipitation because of calcium depletion in the solution, rather than changes to the meteoric and/or marine input. This indicates that a steady state was achieved after sufficient calcium was removed from the brine such that the input flux was equivalent to the output precipitation. Thus, crystallisation took place beneath a stable and persistent pycnocline in marginal Mediterranean water bodies, resulting in near-constant $\delta^{44/40}Ca$ and $^{87}Sr/^{86}Sr$ values within each cycle.

Unlike the lowermost cycles (i.e. 1–5) and the mid-section cycles (i.e. 6–12), the thinner, uppermost gypsum strata (e.g. 13 and 15 cycle) generally show a unidirectional increase in $\delta^{17}O/\delta^{18}O/\delta D$ of basin water and a gradual increase in the Sr/Ca ratio, $\delta^{44/40}Ca$, and $^{87}Sr/^{86}Sr$ values. This suggests that gypsum deposition may have occurred only during certain phases of the precessional cycle, when increased aridity and basin restriction prevailed. This could be due either to environmental conditions not being favourable for gypsum precipitation, or more likely, to calcium limitation and a low Ca^{2+}/SO_4^{2-} ratio in basin waters. During drier periods, reduced riverine input and less weathering of either gypsum or marl deposited in earlier stages would have supplied fewer solutes, particularly calcium, thereby constraining gypsum formation. The weathering of peripheral gypsum and marls may have been enhanced by the progressive shallowing of the basin, along with tectonic uplift. However, it is worth noting that there is also evidence of in-situ carbonate precipitation, at least during certain stages. This is observed, for example, in the interfingered dolomitic marls of the supercones in cycle 10, which outcrop in the Río de Aguas area, where traces of bacterial activity have been identified (Evans et al., 2015).

Whereas the gypsum-marl cycles in the Yesares Member reflect precession (Krijgsman et al., 2001), the

longer-term pattern of modulation of eccentricity by precession is not as apparent in the thickness of beds compared to the underlying Abad Formation. For example, the gypsum supercones facies are deposited during periods of both high and low eccentricity, indicating that their formation is not strictly related to long-term changes in precession forcing. Thus, factors other than tectonic and orbital forcing must be involved in the formation of the differing gypsum facies.

5.2.3 | Glacio-eustatic control on basin hydrology

The latest Miocene (6.26–5.55 Ma) was a time of enhanced glaciation when benthic $\delta^{18}O$ records indicate that ice volume and associated sea level changes were dominantly occurring at a 41-kyr obliquity cycle (Drury et al., 2016; Hodell et al., 2001). Several prominent (Shackleton & Hall, 1997) glacial stages occurred during this time period, including TG24, 22 and TG20 between ~5.9 and ~5.7 Ma. The astronomical tuning of the Site 982 density record to precession permitted a direct bed-to-bed correlation to the Abad Marls and Yesares Member of the Sorbas Basin (Hodell et al., 2001; Krijgsman et al., 2001). A comparison of $\delta^{44/40}Ca$ and $^{87}Sr/^{86}Sr$ in gypsum cycles and $\delta^{18}O$ of the carbonate marls with the benthic $\delta^{18}O$ record of ODP Site 982 (Drury et al., 2018; Hodell et al., 2001) suggests that glacio-eustatic sea-level changes influenced the Mediterranean–Atlantic water exchange during the time of PLG deposition (Figure 9).

Glacio-eustatic changes, superimposed on longer-term tectonic restriction of the Mediterranean-Atlantic exchange, were together responsible for some of the facies and geochemical changes observed in the Sorbas Basin sequence. The appearance of gypsum supercone facies in cycle 6 and a stepped increase in $\delta^{44/40}Ca$ and $^{87}Sr/^{86}Sr$ during the transition from cycle 6 to 7 is linked to the start of a progressive cooling phase, marked by glacial stages TG26 and TG24 and the transition out of an eccentricity minimum phase, indicating a reduction in both seawater and freshwater input due to the modulation of precession by eccentricity. The resultant change in sea level governed by both eustatic variability and eccentricity modulation of precession likely resulted in the fluctuation of the pycnocline associated with the formation of branching gypsum units (Lugli et al., 2010). The $\delta^{44/40}Ca$ and $^{87}Sr/^{86}Sr$ in both the gypsum and the interbedded carbonates (mostly dolomite in cycle 9 to 11; Figure 9) progressively diverge from global ocean values from cycle 7 to 11 during the period of progressive cooling and intensified glaciation and associated sea-level lowering through TG24, 22 and 20. Faster rates of carbonate precipitation corresponding to interbedded marls of cycles 9 to 11 could result in lower $\delta^{44/40}Ca$ values and may be linked to higher degrees of carbonate supersaturation driven by glacio-eustatic changes.

The departure of the $^{87}Sr/^{86}Sr$ from the global oceanic curve over in the upper part of the Sorbas PLG (i.e. cycles 6–12) is also observed in the of $^{87}Sr/^{86}Sr$ profile in PLG deposits from the Vena del Gesso basin (northern Italy; Reghizzi et al., 2018) (Figure 6). However, because of gaps in the Vena del Gesso cycle analysis, the Sr isotope profile does not appear to display the slight reversals in the general trend of decreasing $^{87}Sr/^{86}Sr$ up-section, as observed in the Sorbas PLG. This gradual increase in the $^{87}Sr/^{86}Sr$ values up-section in both marginal basins strongly suggests an increase in the freshwater fraction compared to the seawater fraction because of the restriction of the marginal basins and less water exchange with the open Mediterranean.

Glacial stage TG20 was the largest glaciation during the deposition of the PLG (Hodell et al., 2001) and occurred at a time of low obliquity and when the amplitude of the precession cycle was dampened by low eccentricity. This orbital node is expressed in both the variations in the isotopic composition of gypsum in cycles 9–11, as well as a major change in marl mineralogy from calcite to dolomite during this period (Figure 9). The $^{87}Sr/^{86}Sr$ values of cycles 9–11 display the greatest divergence away from the global ocean curve. Additionally, the progressive increase in carbonate $\delta^{18}O$ and transition from calcite to dolomite in the marls indicate a highly restricted oceanic inflow during cycles 9–11, providing evidence that global sea-level lowering influenced the mineralogy and geochemistry of the gypsum-marl cycles. The terminal supercone cycle and the final step change in $\delta^{44/40}Ca$ and $^{87}Sr/^{86}Sr$ coincide with the termination of TG20, suggesting the minor occurrence of a seawater incursion after this phase (Figure 9).

The non-unidirectional divergence of $\delta^{44/40}Ca$ and $^{87}Sr/^{86}Sr$ supports that glacio-eustatic changes, superimposed on longer-term tectonic restriction of Mediterranean–Atlantic exchange and orbital forcing, were secondarily affecting the geochemical profiles observed in the Yesares Member. After cycle 12 and TG20, global sea level was higher, but the continued tectonic uplift reduced the exchange to a point whereby thick gypsum deposits were prevented from forming in the sequence. As tectonic restriction continued, the gypsum facies disappeared from the upper sequence and were replaced by limestone beds.

5.3 | A proposed mechanism for PLG formation: an orbitally forced calcium flux

An inconsistency exists between the large proportion of freshwater implied from gypsum fluid inclusion and

hydration water isotope ratios during the formation of the PLG and the source of calcium and sulphate ions needed for the formation of such large gypsum deposits. A mechanism other than simple evaporation of seawater is needed to explain the lower salinities inferred from fluid inclusion and isotopic results in the PLG. Bigi et al. (2022) argued post-depositional processes can affect the reliability of the fluid inclusion thermometry analyses that were used in previous studies to infer a relatively low-salinity environment for the deposition of the PLG of the MSC (Aloisi et al., 2022; Evans et al., 2015). However, fluid inclusions analysis is not the only line of evidence supporting a low-salinity fluid for the formation of Messinian gypsum. The presence of centric diatoms inside gypsum crystals (Pellegrino et al., 2021) and the relatively low isotopic ratios of GHW in gypsum support the interpretation of "low salinity gypsum" (Aloisi et al., 2022).

Natalicchio et al. (2014) and Evans et al. (2015) proposed that gypsum formed from a mix of seawater and freshwater enriched in Ca^{2+} and $SO_4{}^{2-}$ by the partial dissolution and recycling of coeval marginal evaporite and carbonate deposits. In contrast, Aloisi et al. (2022) suggested that recycling of older gypsum deposited previously in the basin is unlikely, because no geological evidence supporting this hypothesis has been found to date. However, the up-section trend observed in some of the isotopic proxies obtained from the PLG of the Yesares Member support the input of ions (Ca^{2+}, $SO_4{}^{2-}$, Sr^{2+}, etc.). The $SO_4{}^{2-}/Ca^{2+}$ molar ratio in unevaporated seawater is around 2.7. This means that Ca^{2+} concentration limits gypsum precipitation once depleted. However, the addition of Ca^{2+} may have occurred from different sources, including the weathering of gypsum and marl beds from earlier PLG cycles or carbonate from the Abad member. Also, calcium (Ca^{2+}) delivered by rivers to the Sorbas Basin may have helped maintain the $SO_4{}^{2-}/Ca^{2+}$ molar ratio at levels required for gypsum precipitation. In fact, our measurements of modern springs in the Sierra de los Filabres—likely sources of some of the rivers that once drained into the Sorbas Basin—show Ca^{2+} concentrations of up to 40 ppm.

A late Miocene gypsum deposit that formed solely from the evaporation of seawater has not been found in the Mediterranean yet, and the consistent $^{87}Sr/^{86}Sr$ profiles between differing circum-Mediterranean basins indicate that the original fluids were composed of a large percentage of freshwater. Alternatively, Aloisi et al. (2022) proposed that alternating stratification and mixing of the water column driven by precession and climate oscillation may have resulted in cycles of storage of bacterially reduced sulphur compounds in the deepest parts of the basin (during stratification periods) that oxidised during periods of water column oxygenation. This process could have supplied enough sulphate to provoke saturation in gypsum of the solution and gypsum precipitation that occurred during periods of precession maxima. However, such a mechanism may have resulted in much higher oxygen isotope ratios in the recycled sulphate (Antler et al., 2017), which is not supported by our data or by other published previously datasets of $\delta^{18}O_{SO_4}$ in Messinian gypsum (e.g. Aloisi et al., 2022; García-Veigas et al., 2018).

The increased weathering of carbonate rocks inferred from fluctuations in calcium and strontium isotope ratios provides a potential explanation for the unexpectedly low salinities found within many of the PLG of many Mediterranean marginal basins. Both the solubility of gypsum (K_{sp}) and the product of dissolved calcium [Ca^{2+}] and sulphate [$SO_4{}^{2-}$] determine gypsum precipitation. If $[Ca^{2+}]\times[SO_4{}^{2-}]>K_{sp}$, then gypsum super-saturation is reached and will precipitate. Because normal non-evaporated seawater (0.01 mol L^{-1} [Ca^{2+}], 0.028 mol L^{-1} [$SO_4{}^{2-}$]; $K_{sp}{}^{CaSO_4\cdot 2H_2O}=\sim 0.28\times10^{-3}$) is under-saturated for gypsum ($\sim 2.6\times10^{-3}$) (Broecker & Peng, 1982), evaporation is needed to increase the concentration of dissolved [Ca^{2+}] and [$SO_4{}^{2-}$].

Seawater salinities are required to rise from ~35 ppt to ~130 ppt (Warren, 2016) before gypsum saturation is reached, requiring the loss of ~70% of the starting volume. Once gypsum begins to precipitate, the solution becomes progressively depleted in both calcium and sulphate. However, since the $SO_4{}^{2-}/Ca^{2+}$ molar ratio in unevaporated seawater is approximately 2.7 and calcium carbonate also precipitates during the early stages of evaporation, calcium is depleted from the solution more rapidly than sulphate. By adding [Ca^{2+}], the ion activity product will rise without the need for large amounts of evaporation (Figure S5). The addition of calcium ions from the large-scale weathering of gypsum and carbonates from surrounding catchments will increase the gypsum saturation level at lower salinities.

6 | CONCLUSIONS

Multi-isotope analysis of gypsum and marls from the 15 cycles of the Yesares Member indicate that PLG deposition was influenced by Sorbas Basin hydrology that was affected by tectonics, precession-forced climate oscillations, and eustatic sea-level change. The homogeneous isotopic values recorded in the lower cycles of the sequence suggest hydrological stability and relatively deep waters, whereas these conditions change upwards in the sequence as greater isotopic variability is seen in the upper part of the Yesares Member, suggesting a shallowing trend driven by tectonic restriction. Reversals in the general trend of decreasing Sr isotopes up-section, together with

step changes in Ca isotopes, as well as high $\delta^{18}O_{carb}$ and anomalous mineralogy of the co-occurring marls, indicate glacio-eustatic sea-level variability also affected the seawater input by affecting the inflow of Atlantic seawater. The gypsum of all cycles was formed in a hybrid brine consisting of a seawater body strongly influenced by abundant freshwater input that increased up-section.

ACKNOWLEDGEMENTS

We thank Ian Mather, James Rolfe, and Jason Curtis for laboratory support and technical assistance with stable isotope measurements, Dr. Giulio Lampronti for support with the X-Ray measurements, and Marie Edmonds and David Neave for use of the Linkam THMSG600 cryostage and associated training. This research was supported by funds from the European Research Council under the European Union's Seventh Framework Programme (FP/2007–2013)/ERC Grant Agreement n. 339694 (Water Isotopes of Hydrated Minerals) to D.A. Hodell. This study was supported by project PID2021-123980OA-I00 (GYPCLIMATE), funded by the Ministerio de Ciencia e Innovación of Spain, the Agencia Estatal de Investigación, and the Fondo Europeo de Desarrollo Regional (FEDER). The project "Fortalecimiento de grupos de investigación" P_FORT_GRUPOS_2023/17 of the University of Almería, funded by the Junta de Andalucía Government and Fondos FEDER funds, made possible field sampling. F.G acknowledges the Ramón y Cajal fellowship, RYC2020-029811-I, and the grant PPIT-UAL, Junta de Andalucía-FEDER 2022-2026 (RyC-PPI2021-01). The authors thank the Speleoclub Almería (ECA) for its support during field work in Covadura Cave.

CONFLICT OF INTEREST STATEMENT

The authors declare that they have no known competing financial interests or personal relationships that could have appeared to influence the work reported in this article.

DATA AVAILABILITY STATEMENT

All the data used in this study can be found in Data S1 and Supporting Information.

DEDICATION

Our friend and colleague Judy McKenzie was a staunch advocate of scientific ocean drilling and study of the Messinian Salinity Crisis throughout her long and productive career. Her unbridled enthusiasm for science was contagious, as was her stalwart support for the careers of younger students and colleagues. The authors of this paper include several generations of scientists whose careers were guided—and even crafted—by Judy, who will be forever cherished for her mentorship and friendship.

ORCID

Fernando Gázquez https://orcid.org/0000-0001-8258-1352
David A. Hodell https://orcid.org/0000-0002-8793-162X

REFERENCES

AlKhatib, M. & Eisenhauer, A. (2017) Calcium and strontium isotope fractionation in aqueous solutions as a function of temperature and reaction rate; I. Calcite. *Geochimica et Cosmochimica Acta*, 209, 296–319.

Aloisi, G., Guibourdenche, L., Natalicchio, M., Caruso, A., Haffert, L., El Kilanhy, A. & De la Pierre, F. (2022) The geochemical riddle of "low-salinity gypsum" deposits. *Geochimica et Cosmochimica Acta*, 327, 247–275.

Antler, G., Turchyn, A.V., Ono, S., Sivan, O. & Bosak, T. (2017) Combined ^{34}S, ^{33}S and ^{18}O isotope fractionations record different intracellular steps of microbial sulfate reduction. *Geochimica et Cosmochimica Acta*, 203, 364–380.

Attia, O.E., Lowenstein, T. & Wali, A. (1995) Middle Miocene Gypsum, Gulf of Suez: marine or nonmarine? *SEPM Journal of Sedimentary Research*, 65A(4), 614–626.

Bigi, D., Lugli, S., Manzi, V. & Roveri, M. (2022) Are fluid inclusions in gypsum reliable paleoenvironmental indicators? An assessment of the evidence from the Messinian evaporites. *Geology*, 50(4), 454–459.

Bodnar, R. (1993) Revised equation and table for determining the freezing point depression of H_2ONaCl solutions. *Geochimica et Cosmochimica Acta*, 57(3), 683–684.

Bradbury, H.J., Halloran, K.H., Lin, C.Y. & Turchyn, A.V. (2020) Calcium isotope fractionation during microbially induced carbonate mineral precipitation. *Geochimica et Cosmochimica Acta*, 277, 37–51.

Bradbury, H.J., Torfstein, A., Wong, K. & Turchyn, A.V. (2018) The calcium isotope systematics of the Late Quaternary Dead Sea Basin Lakes. *Geochemistry, Geophysics, Geosystems*, 19(11), 4260–4273.

Bradbury, H.J. & Turchyn, A.V. (2018) Calcium isotope fractionation in sedimentary pore fluids from ODP Leg 175: resolving carbonate recrystallization. *Geochimica et Cosmochimica Acta*, 236, 121–139.

Broecker, W.S. & Peng, T.H. (1982) *Tracers in the Sea*. New York: Eldigio, pp. 1–690.

CIESM. (2008) The Messinian Salinity Crisis from mega-deposits to microbiology—A consensus report. In: Briand, F. (Ed.) *Ciesm workshop monographs*, Monaco, no. 33, p. 168.

Claypool, G.E., Holser, W.T., Kaplan, I.R., Sakai, H. & Zak, I. (1980) The age curves of sulfur and oxygen isotopes in marine sulfate and their mutual interpretation. *Chemical Geology*, 28(1980), 199–260.

De Lange, G.J. & Krijgsman, W. (2010) Messinian Salinity Crisis: a novel unifying shallow gypsum/deep dolomite formation mechanism. *Marine Geology*, 275(1–4), 273–277.

Dela Pierre, F., Clari, P., Natalicchio, M., Ferrando, S., Giustetto, R., Lozar, F., Lugli, S., Manzi, V., Roveri, M. & Violanti, D. (2014) Flocculent layers and bacterial mats in the mudstone interbeds of the Primary Lower Gypsum unit (Tertiary Piedmont basin, NW Italy): archives of palaeoenvironmental changes during the Messinian Salinity Crisis. *Marine Geology*, 355, 71–87.

Deuβen, K., Voigt, C., Staubwasser, M., Münker, C., El-Shenawy, M., Klipsch, S. & Herwartz, D. (2024) Hydroclimate of the Messinian Salinity Crisis constrained from paleo-water triple oxygen, hydrogen, and strontium isotopes. *Geochimica et Cosmochimica Acta*, 375, 134–145.

Do Couto, D., Gumiaux, C., Augier, R., Lebret, N., Folcher, N., Jouannic, G., Jolivet, L., Suc, J.-P. & Gorini, C. (2014) Tectonic inversion of an asymmetric graben: insights from a combined field and gravity survey in the Sorbas basin. *Tectonics*, 33(7), 1360–1385.

Dronkert, H. (1985) Evaporite models and sedimentology of Messinian and recent evaporites. In: GUA Papers of Geology, Series 1, No. 24, 283.

Drury, A.J., John, C.M. & Shevenell, A.E. (2016) Evaluating climatic response to external radiative forcing during the late Miocene to early Pliocene: new perspectives from eastern equatorial Pacific (IODP U1338) and North Atlantic (ODP 982) locations. *Paleoceanography*, 31, 167–184.

Drury, A.J., Westerhold, T., Hodell, D. & Röhl, U. (2018) Reinforcing the North Atlantic backbone: revision and extension of the composite splice at ODP Site 982. *Climate of the Past*, 14(3), 321–338.

Engleman, E.E., Jackson, L.L. & Norton, D.R. (1985) Determination of carbonate carbon in geological materials by coulometric titration. *Chemical Geology*, 53, 125–128.

Evans, N.P., Bauska, T.K., Gázquez-Sánchez, F., Brenner, M., Curtis, J.H. & Hodell, D.A. (2018) Quantification of drought during the collapse of the classic Maya civilization. *Science*, 361(6401), 498–501.

Evans, N.P., Turchyn, A.V., Gázquez, F., Bontognali, T.R., Chapman, H.J. & Hodell, D.A. (2015) Coupled measurements of $\delta^{18}O$ and δD of hydration water and salinity of fluid inclusions in gypsum from the Messinian Yesares Member, Sorbas Basin (SE Spain). *Earth and Planetary Science Letters*, 430, 499–510.

Flecker, R., De Villiers, S. & Ellam, R.M. (2002) Modelling the effect of evaporation on the salinity-$^{87}Sr/^{86}Sr$ relationship in modern and ancient marginal-marine systems: the Mediterranean Messinian Salinity Crisis. *Earth and Planetary Science Letters*, 203, 221–233.

Flecker, R. & Ellam, R.M. (2006) Identifying Late Miocene episodes of connection and isolation in the Mediterranean-Paratethyan realm using Sr isotopes. *Sedimentary Geology*, 188-189, 189–203.

Flecker, R., Krijgsman, W., Capella, W., de Castro Martins, C., Dmitrieva, E., Mayser, J.P., Marzocchi, A., Modestu, S., Ochoa, D., Simon, D., Tulbure, M., van den Berg, B., van der Schee, M., de Lange, G., Ellam, R., Govers, R., Gutjahr, M., Hilgen, F., Kouwenhoven, T., Lofi, J., Meijer, P., Sierro, F.J., Bachiri, N., Barhoun, N., Alami, A.C., Chacon, B., Flores, J.A., Gregory, J., Howard, J., Lunt, D., Ochoa, M., Pancost, R., Vincent, S. & Yousfi, M.Z. (2015) Evolution of the Late Miocene Mediterranean-Atlantic gateways and their impact on regional and global environmental change. *Earth-Science Reviews*, 150, 365–392.

García-Veigas, J., Cendón, D.I., Gibert, L., Lowenstein, T.K. & Artiaga, D. (2018) Geochemical indicators in Western Mediterranean Messinian evaporites: implications for the salinity crisis. *Marine Geology*, 403, 197–214.

Gázquez, F., Calaforra, J.M., Evans, N.P. & Hodell, D.A. (2017) Using stable isotopes ($\delta^{17}O$, $\delta^{18}O$ and δD) of gypsum hydration water to ascertain the role of water condensation in the formation of subaerial gypsum speleothems. *Chemical Geology*, 452, 34–46.

Gázquez, F., Calaforra, J.M. & Fernández-Cortés, A. (2016) Flash flood events recorded by air temperature changes in caves: a case study in Covadura Cave (SE Spain). *Journal of Hydrology*, 541, 136–145.

Gázquez, F., Evans, N.P. & Hodell, D.A. (2017) Precise and accurate isotope fractionation factors ($\alpha^{17}O$, $\alpha^{18}O$ and αD) for water and $CaSO_4{\cdot}2H_2O$ (gypsum). *Geochimica et Cosmochimica Acta*, 198, 259–270.

Gázquez, F. & Hodell, D.A. (2022) Preservation and modification of the isotopic composition ($^{18}O/^{16}O$ and $^{2}H/^{1}H$) of structurally-bound hydration water of gypsum ($CaSO_4{\cdot}2H_2O$) in aqueous solution. *Geochimica et Cosmochimica Acta*, 337, 73–81.

Gázquez, F., Mather, I., Rolfe, J., Evans, N.P., Herwartz, D., Staubwasser, M. & Hodell, D.A. (2015) Simultaneous analysis of $^{17}O/^{16}O$, $^{18}O/^{16}O$ and $^{2}H/^{1}H$ of gypsum hydration water by cavity ringdown laser spectroscopy. *Rapid Communications in Mass Spectrometry*, 29(21), 1997–2006.

Gázquez, F., Morellón, M., Bauska, T., Herwartz, D., Surma, J., Moreno, A., Staubwasser, M., Valero-Garcés, B., Delgado-Huertas, A. & Hodell, D.A. (2018) Triple oxygen and hydrogen isotopes of gypsum hydration water for quantitative paleohumidity reconstruction. *Earth and Planetary Science Letters*, 481, 177–188.

Goldstein, R.H. & Reynolds, T.J. (1994) Systematics of fluid inclusions in diagenetic minerals. In: *SEPM short course 31*. Tulsa, OK, USA: Society for Sedimentary Geology, p. 199.

Harouaka, K., Eisenhauer, A. & Fantle, M.S. (2014) Experimental investigation of Ca isotopic fractionation during abiotic gypsum precipitation. *Geochimica et Cosmochimica Acta*, 129, 157–176.

Herwartz, D., Surma, J., Voigt, C., Assonov, S. & Staubwasser, M. (2017) Triple oxygen isotope systematics of structurally bonded water in gypsum. *Geochimica et Cosmochimica Acta*, 209, 254–266.

Hodell, D.A., Curtis, J.H., Sierro, F.J. & Raymo, M.E. (2001) Correlation of late Miocene to early Pliocene sequences between the Mediterranean and North Atlantic. *Paleoceanography*, 16, 164–178.

Hsü, K.J., Ryan, W.B.F. & Cita, M.B. (1973) Late Miocene desiccation of the Mediterranean. *Nature*, 242(5395), 240–244.

Krijgsman, W., Capella, W., Simon, D., Hilgen, F.J., Kouwenhoven, T.J., Meijer, P.T., Sierro, F.J., Tulbure, M.A., van den Berg, B.C., van der Schee, M. & Flecker, R. (2018) The Gibraltar Corridor: watergate of the Messinian Salinity Crisis. *Marine Geology*, 403, 238–246.

Krijgsman, W., Fortuin, A.R., Hilgen, F.J. & Sierro, F.J. (2001) Astrochronology for the Messinian Sorbas basin (SE Spain) and orbital (precessional) forcing for evaporite cyclicity. *Sedimentary Geology*, 140(1–2), 43–60.

Krijgsman, W., Hilgen, F.J., Raffi, I., Sierro, F.J. & Wilson, D.S. (1999) Chronology, causes and progression of the Messinian Salinity Crisis. *Nature*, 400, 652–655.

Krijgsman, W. & Meijer, P.T. (2008) Depositional environments of the Mediterranean "Lower Evaporites" of the Messinian salinity crisis: constraints from quantitative analyses. *Marine Geology*, 253(3-4), 73–81.

Krijgsman, W., Rohling, E.J., Palcu, D.V., Raad, F., Amarathunga, U., Flecker, R., Florindo, F., Roberts, A.P., Sierro, F.J. & Aloisi,

G. (2024) Causes and consequences of the Messinian Salinity Crisis. *Nature Reviews Earth and Environment*, 5, 335–350.

Laskar, J., Robutel, P., Joutel, F., Gastineau, M., Correia, A.C.M. & Levrard, B. (2004) A long-term numerical solution for the insolation quantities of the Earth. *Astronomy & Astrophysics*, 428(1), 261–285.

Liu, T., Artacho, E., Gázquez, F., Walters, G. & Hodell, D.A. (2019) Prediction of equilibrium isotopic fractionation of the gypsum/bassanite/water system using first-principles calculations. *Geochimica et Cosmochimica Acta*, 244, 1–11.

Lofi, J., Sage, F., Deverchere, J., Loncke, L., Maillard, A., Gaullier, V., Thinon, I., Gillet, H., Guennoc, P. & Gorini, C. (2011) Refining our knowledge of the Messinian Salinity Crisis records in the offshore domain through multi-site seismic analysis. *Bulletin De La Société Géologique De France*, 182(2), 163–180.

Longinelli, A. (1979) Isotope geochemistry of some Messinian evaporates: paleoenvironmental implications. *Palaeogeography, Palaeoclimatology, Palaeoecology*, 29, 95–123.

Lu, F.H. & Meyers, W.J. (2003) Sr, S, and $O(SO_4)$ isotopes and the depositional environments of the upper Miocene Evaporites, Spain. *Journal of Sedimentary Research*, 73, 444–450.

Lugli, S., Bassetti, M.A., Manzi, V., Barbieri, M., Longinelli, A. & Roveri, M. (2007) The Messinian 'Vena del Gesso' evaporites revisited: characterization of isotopic composition and organic matter. *Geological Society, London, Special Publications*, 285(1), 179–190.

Lugli, S., Manzi, V., Roveri, M. & Schreiber, C.B. (2010) The Primary Lower Gypsum in the Mediterranean: a new facies interpretation for the first stage of the Messinian Salinity Crisis. *Palaeogeography, Palaeoclimatology, Palaeoecology*, 297(1), 83–99.

Manzi, V., Gennari, R., Hilgen, F., Krijgsman, W., Lugli, S., Roveri, M. & Sierro, F.J. (2013) Age refinement of the Messinian Salinity Crisis onset in the Mediterranean. *Terra Nova*, 25(4), 315–322.

McArthur, J., Howarth, R. & Bailey, T. (2001) Strontium isotope stratigraphy: LOWESS version 3: best fit to the marine Sr-isotope curve for 0-509 Ma and accompanying look-up table for deriving numerical age. *The Journal of Geology*, 109(2), 155–170.

Modestou, S., Simon, D., Gutjahr, M., Marzocchi, A., Kouwenhoven, T.J., Ellam, R.M. & Flecker, R. (2017) Precessional variability of $^{87}Sr/^{86}Sr$ in the late Miocene Sorbas Basin: an interdisciplinary study of drivers of interbasin exchange. *Paleoceanography*, 32, 531–552.

Müller, D.W. & Mueller, P.A. (1991) Origin and age of the Mediterranean Messinian evaporites: implications from Sr isotopes. *Earth and Planetary Science Letters*, 107(1), 1–12.

Natalicchio, M., Dela Pierre, F., Lugli, S., Lowenstein, T.K., Feiner, S.J., Ferrando, S., Manzi, V., Roveri, M. & Clari, P. (2014) Did Late Miocene (Messinian) gypsum precipitate from evaporated marine brines? Insights from the Piedmont Basin (Italy). *Geology*, 42(3), 179–182.

Nielsen, L.C., DePaolo, D.J. & De Yoreo, J.J. (2012) Self-consistent ion-by-ion growth model for kinetic isotopic fractionation during calcite precipitation. *Geochimica et Cosmochimica Acta*, 86, 166–181.

Ochoa, D., Sierro, F.J., Lofi, J., Maillard, A., Flores, J.A. & Suárez, M. (2015) Synchronous onset of the Messinian evaporite precipitation: first Mediterranean offshore evidence. *Earth and Planetary Science Letters*, 427, 112–124.

Palmer, M.R. & Edmond, J.M. (1992) Controls over the strontium composition of river water. *Geochimica et Cosmochimica Acta*, 56, 2099–2111.

Pellegrino, L., Natalicchio, M., Abe, K., Jordan, R.W., Favero-Longo, S.E., Ferrando, L.S., Carnevale, G. & Dela Pierre, F. (2021) Tiny, glassy, and rapidly trapped: the nano-sized planktic diatoms in Messinian (late Miocene) gypsum. *Geology*, 49(11), 1369–1374.

Reghizzi, M., Gennari, R., Doubille, E., Lugli, S., Manzi, V., Paolo, M., Roveri, M., Sierro, F.J. & Marco, T. (2017) Isotope stratigraphy ($^{87}Sr/^{86}Sr$, $\delta^{18}O$, $\delta^{13}C$) of the Sorbas basin (Betic Cordillera, Spain): paleoceanographic evolution across the onset of the Messinian Salinity Crisis. *Palaeogeography, Palaeoclimatology, Palaeoecology*, 469, 60–73.

Reghizzi, M., Lugli, S., Manzi, V., Rossi, F.P. & Roveri, M. (2018) Orbitally forced hydrological balance during the Messinian Salinity Crisis: insights from strontium isotopes ($^{87}Sr/^{86}Sr$) in the Vena del Gesso Basin (Northern Apennines, Italy). *Paleoceanography and Paleoclimatology*, 33(7), 716–731.

Rosell, L., Orti, F., Kasprzyk, A., Playa, E. & Peryt, T.M. (1998) Strontium geochemistry of Miocene primary gypsum; Messinian of southeastern Spain and Sicily and Badenian of Poland. *Journal of Sedimentary Research*, 68(1), 63–79.

Rossi, C., Vilas, L. & Arias, C. (2015) The Messinian marine to non-marine gypsums of Jumilla (Northern Betic Cordillera, SE Spain): isotopic and Sr concentration constraints on the origin of parent brines. *Sedimentary Geology*, 328, 96–114.

Roveri, M., Flecker, R., Krijgsman, W., Lofi, J., Lugli, S., Manzi, V., Sierro, F.J., Bertini, A., Camerlenghi, A., De Lange, G., Govers, R., Hilgen, F.J., Hübscher, C., Meijer, P.T. & Stoica, M. (2014) The Messinian Salinity Crisis: past and future of a great challenge for marine sciences. *Marine Geology*, 352, 25–58.

Roveri, M., Gennari, R., Lugli, S. & Manzi, V. (2009) The Terminal Carbonate Complex: the record of sea-level changes during the Messinian Salinity Crisis. *Geoacta*, 8, 63–77.

Ryan, W.B.F., Hsü, K.J., Cita, M.B., Dumitrica, P., Llort, J., Maync, W., Nesteroff, W.D., Pautot, G., Stradner, H. & Wezel, F.C. (1973) Sites 133 and 134. In: Ryan, W.B.F., Hsu, K.J., Cita, M.B. (Eds.) *Initial reports of the deep sea drilling project, 13*, Vol. XIII. Washington, D.C.: U.S. Government Printing Office, pp. 465–514.

Ryan, W.B.F. & Raad, F. (2025) Introducing a water activity coefficient to account for abundance and isotopic compositions of gypsum and halite in the Mediterranean's salt giant deposit. *Sedimentary Geology*, 481, 106876.

Shackleton, N.J. & Hall, M.A. (1997) The late Miocene stable isotope record, Site 926. In: Shackleton, N.J., Curry, W.B., Richter, C. & Bralower, T.J. (Eds.) *Proceedings of the Ocean Drilling Program, Scientific Results, 154*. College Station, TX, USA: Ocean Drilling Program, pp. 367–373.

Sierro, F., Hilgen, F., Krijgsman, W. & Flores, J. (2001) The Abad composite (SE Spain): a Messinian reference section for the Mediterranean and the APTS. *Palaeogeography, Palaeoclimatology, Palaeoecology*, 168(1–2), 141–169.

Simon, D., Marzocchi, A., Flecker, R., Lunt, D.J., Hilgen, F.J. & Meijer, P.T. (2017) Quantifying the Mediterranean freshwater budget throughout the late Miocene: new implications for sapropel formation and the Messinian Salinity Crisis. *Earth and Planetary Science Letters*, 472, 25–37.

Simon, D. & Meijer, P.T. (2017) Salinity stratification of the Mediterranean Sea during the Messinian crisis: a first model analysis. *Earth and Planetary Science Letters*, 479, 366–376.

Spötl, C. & Vennemann, T.W. (2003) Continuous-flow isotope ratio mass spectrometric analysis of carbonate minerals. *Rapid Communications in Mass Spectrometry*, 17, 1004–1006.

Surma, J., Assonov, S., Herwartz, D., Voigt, C. & Staubwasser, M. (2018) The evolution of ^{17}O-excess in surface water of the arid environment during recharge and evaporation. *Scientific Reports*, 8, 4972.

Topper, R.P.M., Lugli, S., Manzi, V., Roveri, M. & Meijer, P.T. (2014) Precessional control of Sr ratios in marginal basins during the Messinian Salinity Crisis? *Geochemistry, Geophysics, Geosystems*, 15(5), 1926–1944.

Topper, R.P.M. & Meijer, P.T. (2013) A modeling perspective on spatial and temporal variations in Messinian evaporite deposits. *Marine Geology*, 336, 44–60.

Valetti, L., Rutter, E., McCabe, A. & Mecklenburgh, J. (2019) On the structure and evolution of the Sorbas basin, S.E. Spain. *Tectonophysics*, 773, 228230.

Voigt, C., Herwartz, D., Dorador, C. & Staubwasser, M. (2021) Triple oxygen isotope systematics of evaporation and mixing processes in a dynamic desert lake system. *Hydrology and Earth System Sciences*, 25, 1211–1228.

Warren, J.K. (2016) Depositional chemistry and hydrology. In: *Evaporites*. Cham: Springer International Publishing, pp. 85–205.

SUPPORTING INFORMATION

Additional supporting information can be found online in the Supporting Information section at the end of this article.

How to cite this article: Gázquez, F., Evans, N.P., Bauska, T.K., Bradbury, H.J., Turchyn, A.V., del Carmen Barroso, M. et al. (2026) Orbital and eustatic control of basin hydrology during the first stage of the Messinian Salinity Crisis. *The Depositional Record*, 12, e70045. Available from: https://doi.org/10.1002/dep2.70045